Title
Microstructural design of soft magnetic CoFe - based alloys with targeted magnetic and electronic properties for transformer cores

Permalink
https://escholarship.org/uc/item/7545k743

Author
Belcher, Calvin Harris

Publication Date
2021

UNIVERSITY OF CALIFORNIA,

IRVINE

Microstructural design of soft magnetic CoFe – based alloys with targeted magnetic and electronic properties for transformer cores

THESIS

submitted in partial satisfaction of the requirements for the degree of

MASTER OF SCIENCE

in Materials Science and Engineering

by

Calvin Harris Belcher

Thesis Committee:
Professor Diran Apelian,Chair
Professor Julie M. Schoenung
Professor Timothy J. Rupert

2021

TABLE OF CONTENTS

Page

LIST OF FIGURES

LIST OF TABLES

ACKNOWLEDGEMENTS

First of all, I must acknowledge and give many thanks to my incredible advisors, Dr. Enrique J. Lavernia and Dr. Diran Apelian. During my time as a graduate student at UC Irvine, Enrique and Diran have guided and supported me in this thesis research, the writing process, and my growth as a materials scientist. I owe much of my success as a graduate student and leader to the both of them. I would also like to thank and acknowledge my collaborator in this thesis research, Dr. Todd Monson of Sandia National Laboratories. Although not required of him, Todd has filled a role as an additional advisor, guiding and supporting me through the research process in this thesis from a fundamental physics perspective outside my own metallurgical training. I must also acknowledge Dr. Benjamin E. MacDonald, who, when I first met him, was an invaluable graduate student mentor to the start of my career in research as an undergraduate and taught me the innerworkings of graduate research. Now a postdoctoral scientist, Ben has continued to provide mentorship to me, even when not required. Ben has provided significant guidance and insight to my abilities as a researcher and writer and enhanced the quality of this thesis and my writing in general. Beyond the scope of research and a scientific career, Ben's actions and attitudes have instilled in me qualities necessary to develop my own sense of a meaningful life I can fully appreciate. I would also like to thank Darryl Mack for his technical support and insight throughout my research career as a student. Darryl's constant development of productive, safe, and well thought laboratory spaces have enabled myself and many other researchers to conduct quality research experiments. During my time as a student, Darryl's upbeat attitude and intuition across disciplines drove me to think critically when designing and working with mechanical systems. I am proud to have each of these accomplished scientists as my mentors in research and in life and

I look forward to continuing my growth as a materials scientist and leader with their continued guidance through my PhD program.

My deepest thanks are also extended to my M.S. Thesis committee members Dr. Julie Schoenung and Dr. Timothy Rupert. Julie and Tim have been invaluable voices and educators throughout my time as a student at UCI. At the end of this thesis research, Tim stepped in as a temporary advisor to me and provided insight to enhance the quality of this thesis research I am deeply thankful for. I am incredibly grateful for the constant leadership and insight provided by Julie. Sharing lab spaces with Julie's research group members allowed me experience and appreciate her care for the students she works with.

I would like to also acknowledge the members of Enrique, Diran, and Julie's groups who I have had the opportunity to collaborate with and learn from. I am grateful for the opportunity to work with such a supportive and caring group of people. I must first acknowledge Stoney Middleton, Dr. Umberto Bertoli, Dr. James Haley, Dr. Parnian Kiani, and Dr. Xin Wang who have since graduated and left the groups, but had roles in supporting and mentoring me as an undergraduate and graduate researcher. I must also deeply thank Dr. Baolong Zheng, Dr. Alex Dupuy, and Dr. Yizhang Zhou in particular, for introducing me to the research in this thesis and for mentoring me through the early stages and trainings necessary for this thesis research. I look forward to continuing my growth as a materials scientist with Katie Acord, Sasha Vyatskikh, Kehang Yu, Arturo Meza, Sen Jiang, Justin Cortez, Salma El-Azab, and Sakshi Bajpai in our PhD programs. I have truly enjoyed working with this group and am excited for all of our futures.

I would like to acknowledge the support from ARPA-E (DE-AR0001020) for the various studies described in this thesis. I would also like to again deeply thank our collaborator, Dr. Todd

Monson and Sandia National Laboratories for providing guidance and mentorship for this thesis research as well as the tools for the functional properties measurements. I must also thank the staff of the UCI IMRI and LEXI facilities for their management and trainings of the key materials characterization tools used throughout this thesis research.

ABSTRACT

Microstructural design of soft magnetic CoFe – based alloys with targeted magnetic and electronic properties for transformer cores

by

Calvin Harris Belcher
Master of Science in Materials Science and Engineering
University of California, Irvine, 2021
Professor Diran Apelian, Chair

As the world's need for electrical power grows, so too does the need for more efficient transformers and transformer cores to properly transmit and store power across large grids and distances. There is also an additional need for transformers that are more resilient to events such as electromagnetic pulse (EMP) and geomagnetic disturbances (GMD). The objective of this research is to use microstructural design approaches to develop CoFe – based soft magnetic materials for more resilient and efficient transformer cores. The studies presented here implement the use of non-equilibrium powder metallurgical processing techniques to design and fabricate microstructures necessary for efficient magnetic and electronic properties in transformer cores such as high saturation magnetic polarization and high electrical resistivity. The first study aimed to develop CoFe – P alloys with unstable nanocrystalline, solid solution microstructures and discusses the effect of a secondary intermetallic phase on the saturation magnetic polarization and electrical resistivity of the bulk alloy. Solid solution CoFe – P alloy powders were prepared by mechanically alloying metal powders; however, our results revealed the formation of a stable secondary phase occurred during spark plasma sintering (SPS) consolidation at relatively high temperatures. The magnetic properties of the precipitated intermetallic phase were found to be detrimental to the soft magnetic properties of the targeted CoFe – P alloy. In the second study, the columnar grain microstructures of additively manufactured CoFe are discussed with respect to the magnetocrystalline anisotropy of the B2 ordered BCC CoFe structure. Additive manufacturing holds potential as a key manufacturing process for brittle alloys such as CoFe and the microstructural control of additive manufacturing processes can enable the development of textured CoFe alloys for more efficient soft magnetic properties. Despite the columnar grains, the magnetic behavior of additively manufactured CoFe alloys was measured to be isotropic. The isotropic magnetic behavior was attributed to randomly oriented columnar grains, not textured, which were attributed to the 90° hatch rotation parameter used during the additive manufacturing process. The final study assesses the microstructural development of a CoFe – based soft magnetic composite with a continuous non-magnetic Al_2O_3 phase fully intersecting CoFe phase particles to produce a composite with high saturation magnetic polarization and high electrical resistivity. The CoFe – Al_2O_3 composite was developed by coating CoFe particles with Al_2O_3 and subsequently consolidating them using spark plasma sintering. Upon consolidation at relatively high temperature, the CoFe was found to diffuse into the Al_2O_3 coatings at the particle boundaries and was attributed to low resistivity in the composite. However, at lower consolidation temperature, diffusion of CoFe was not observed and a high electrical resistivity was achieved, while maintaining a high magnetic polarization. Together, these studies represent effective microstructural design approaches to the CoFe system of materials to develop more efficient and resilient soft magnetic transformer cores.

Chapter 1: Introduction to the design of soft magnetic materials for transformer cores

1.1. Background on electrical transformers

Buildings, transportation, and power grids around the world rely on power conversion devices such as transformers, motors, and inductors to convert electrical power. While motors convert electrical power to mechanical power and inductors transfer and store electrical power in circuits, transformers are necessary for converting electrical power by stepping up or down voltages between power generation, power transmission sources (e.g., high voltage power lines), and end user applications. To transmit power across miles of power lines, high voltages on the order of tens of kV are required, but most appliances in buildings and homes safely operate with low voltages on the order of one hundred V. Voltage steps across transformers are necessary to deliver lower voltages to end user applications on power grids while also allowing efficient, large-scale transmission of electrical power across miles of high voltage power lines.

Fundamentally, transformers rely on the application of Ampere's Law to step up or down voltages [1]. A schematic of the typical design of a transformer core is presented in Figure 1 below.

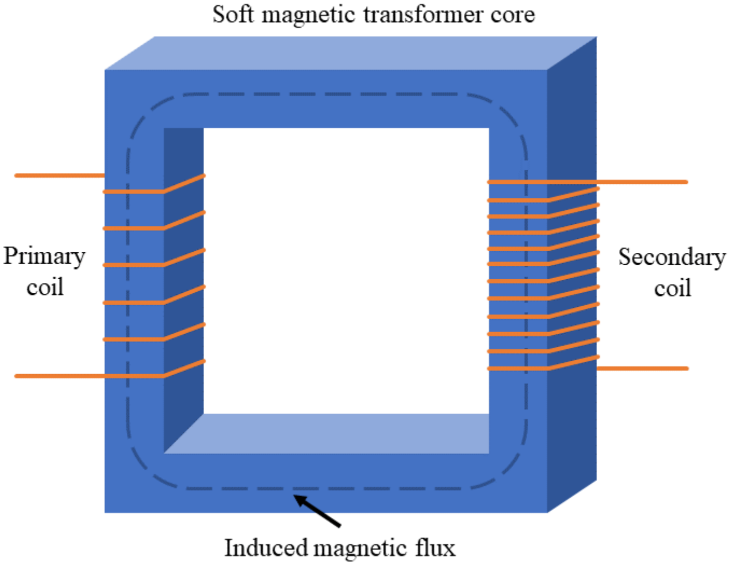

Figure 1. Schematic diagram of a transformer core, the induced magnetic flux, and the primary and secondary coils needed to step up or down voltages.

This schematic shows the transformer core, typically in a toroid or toroid-like geometry, and the primary and secondary coils wound of conductive wire. When stepping down voltage, the high voltage alternating current from power transmission lines is applied through the primary coil, which then induces a switching magnetic flux through the transformer core material. The switching magnetic flux, in turn, generates an alternating current in the secondary winding with a lower voltage ideal for the end user. To tailor an exact voltage step across the transformer, the number of windings in the primary and secondary coils can be varied. While varying the number of coil windings can finely tune voltage step adjustments, relatively large voltage steps require larger transformer cores to sustain the increased accompanying magnetic inductance [2]. Depending on the voltage step needed and the total volt-amp (VA) power rating of a transformer's core material, a transformer can range from as small as the tip of a finger to as large as a room. The efficiency of a transformer is derived from the core's ability to be magnetized and demagnetized, so the core must be made of a soft magnetic material. The term soft does not imply soft magnetic transformer core materials are mechanically soft, but instead refers to the core materials' soft magnetism, meaning the direction of the magnetic polarity in the core can be switched back and forth with relative ease. This back and forth switching of the magnetic polarity is enabled by the relatively low magnetic coercivity, (H_c) or the ability to resist an external magnetic field, of soft magnetic materials and has driven their use in transformer cores. Ultimately, the world's power grids rely on transformers and the properties of their soft magnetic cores to efficiently transmit, convert, and deliver electrical power across large distances.

Currently, the limited efficiency of transformer cores is associated with significant electrical energy losses around the world. As of 2019, in the U.S. alone, 7% of electricity generated was lost to transmission and distribution, according to the U.S. Energy Information Administration (EIA)

[3]–[5]. According to Leary et al, the U.S. EIA documented energy losses from 1949 - 2010 cost a total of $25.8 billion in the U.S. and that number grows as demand for power also increases [6]. The high costs and energetic losses associated with transformer operation and soft magnetic transformer cores drives the need for novel core materials with improved efficiency.

1.2. Properties of soft magnetic materials used as transformer cores

Soft magnetic materials are used in the manufacture of transformer cores due to their ability to be magnetized and demagnetized. The measure of this property is known as coercivity, which is the amount of applied magnetic field needed to bring the induced magnetic field in the material to zero. As opposed to hard or permanent magnets which possess high coercivity values, soft magnets have a H_c less than the Earth's magnetic field ($H_c < 1000$ A/m). The low coercivity of soft magnetic materials enables their use in transformers and other alternating current power conversion applications. The lower coercivity in a soft magnetic core material allows for energetically easier switching of the induced magnetic polarity and reduces the magnetic core losses associated with the applied field overcoming the coercivity in the core material [7], [8]. Achieving high permeability (μ) in soft magnetic materials also reduces magnetic losses during transformer core operation. The μ of a soft magnetic material is a measure of the total magnetic induction of the material, with respect to the applied field and is generally inversely related to H_c. The μ is often reported as a unitless relative permeability (μ_r), a ratio of μ to the permeability of free space (μ_0). One of the other major sources of power losses in soft magnetic core materials is eddy current losses. Eddy currents are eddies, or loops, of electrical current produced in conductive materials by a switching magnetic field. Eddy currents can be produced by the induced magnetic field in the core material during operation and consequently take energy away from the magnetization processes in soft magnetic core materials. From Equation 1 below,

$$P_e \propto \frac{d^2 B^2 f^2}{\rho}, \quad (1)$$

eddy current losses (P_e) are inversely proportional to the electrical resistivity (ρ) of the bulk material. *B* is the magnetic induction, *f* is the frequency of operation of the transformer, and *d* is the electrical domain size, or effective scale of eddy currents, and sometimes sheet thickness for laminated transformer core materials [9]. By increasing the resistivity of the bulk material, the production of eddy currents can be minimized, thereby minimizing eddy current losses. Typical soft magnetic cores have resistivity on the order of ~0.1 μΩ·m and increasing the resistivity of these materials by several orders of magnitude can reduce losses associated with power conversion and save billions of dollars annually [10]. Many soft magnetic material design approaches have been developed to achieve cores with high resistivity. For example, by laminating thin sheets of soft magnetic material, individual sheets are insulated from each other, effectively reducing the effective size of the eddy currents produced in the core. Despite these approaches, because most soft magnetic materials are metallic and contain high concentrations of ferromagnetic metal elements such as Co, Fe and Ni, they typically have low resistivity, posing a challenge to the field: to design a soft magnetic metal alloy with high resistivity.

In soft magnetic transformer cores, an applied field from an alternating electric current induces the magnetic flux necessary for operation of the core. As the magnitude of the applied magnetic field increases, so too does the magnitude of the induced magnetic field in the soft magnetic transformer core. At a certain point, a saturation magnetization (M_s), or saturation magnetic polarization (J_s), is reached, where the induced field in the soft magnetic material no longer increases with the magnitude of the applied field. From Equation 2 below,

$$J_s = \mu_0 \cdot B, \quad (2)$$

J_s is calculated from the product of μ_0, the permeability of free space, and B, the magnetic induction in the magnetic material [9]. The J_s limits the amount of power that a given transformer core size can convert or sustain. With a higher J_s, a transformer could perform with a higher power density, allowing that core to be manufactured in smaller sizes while still performing at the same power storage and conversion capacities. Typical J_s values of transformer core materials are on the order of ~1.9 T. But by targeting a J_s above 2.0 T, higher power densities in transformers and motors can be achieved, cutting manufacturing and raw material costs, and improving power conversion efficiency [7], [8], [11]. As shown in previous literature and in the Slater – Pauling relationship, the highest reported values of J_s are obtained by CoFe based alloys with low concentrations of alloying elements due to their electron spin-orbit interactions [9], [10]. However, this alloy system has relatively low electrical resistivity and has driven much of the compositional space explored by transformer core research. In designing new, more cost efficient soft magnetic materials for transformer cores, the goal of the field is to produce a bulk material with both high J_s and high resistivity. Unfortunately, design approaches to improve the resistivity of soft magnetic materials are often accompanied by detrimental decreases to the material's J_s [6], [8], [9]. Improving both of these properties – high saturation magnetic polarization and high electrical resistivity of soft magnetic materials for transformer cores is necessary for more sustainable energy practices and conversion across the world.

1.3. Progress in soft magnet materials used as transformer cores

In the past 100 years that transformers have existed, Si-steels quickly emerged as an efficient and economic material for transformer cores. Development of transformers began in the 1880s. While several scientists simultaneously developed transformer-like devices around the world, the first device named as a "transformer" was developed by Otto Blathy of Italy in 1885 [12], [13].

This initial transformer had a toroidal core made of iron. The original iron cores were improved upon by laminating sheets of iron with insulation between sheets to reduce eddy current losses. In the early 1900s, more efficient magnetic and electronic properties and relatively inexpensive manufacturing processes paved the way for laminated grain-oriented Si steel sheets to replace the laminated iron cores. Despite decades of advancements in metallurgical processing and alloy design, to this day, grain-oriented Si-steels are still the most widely used soft magnetic transformer core material.

The transformer core market has been dominated by grain-oriented Si-steels since the early 1900s thanks to their moderate balance of J_s and electrical resistivity and relatively inexpensive manufacturing costs [7], [14], [15]. As shown in Figure 2 from Ouyang et al., Si-steels are labeled as Fe3.2Si and Fe6.5Si and have a J_s of approximately 1.8 to 2.0 T and a resistivity of around 0.5 to 0.8 μΩ·m [15].

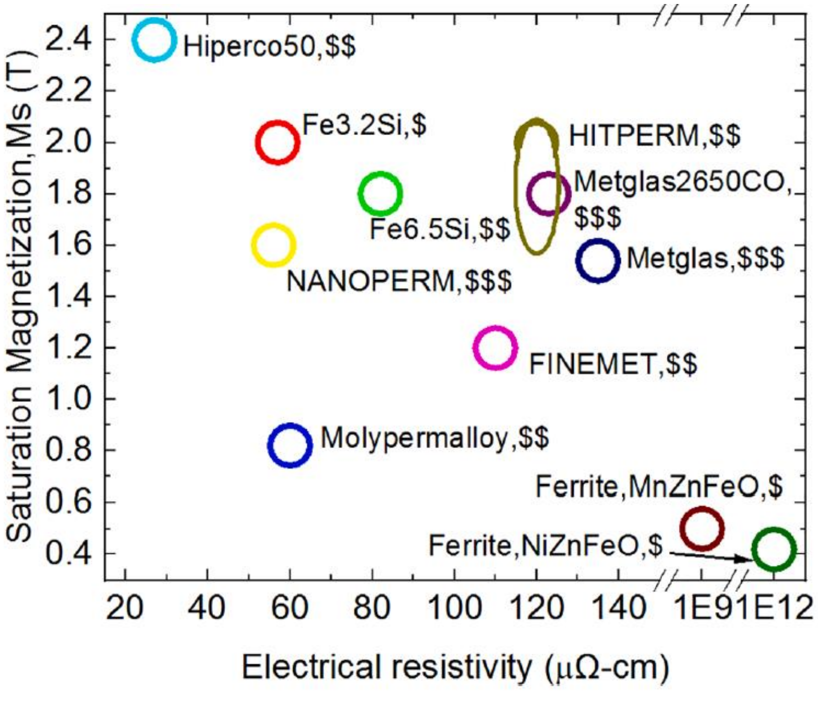

Figure 2. Comparison of saturation magnetization and electrical resistivity of various soft magnetic materials developed recently for transformer core applications, reprinted from Ouyang et al [15].

The Fe3.2Si and Fe6.5Si labels denote the amount of Si alloyed in Fe. The 3.2 wt. % Si in Fe is the more common Si-steel, and the newly developed 6.5 wt. % Si in Fe alloy is an emerging material. While Si-steels do not have the highest reported individual J_s or electrical resistivity, Si-steels offer the best combination of the two properties (shown in Figure 2) at a competitive manufacturing cost, as denoted by the $ symbol. In grain-oriented Si-steels, a relatively high J_s is achieved by the crystallographic texture and ferromagnetic B2 ordered body centered cubic (BCC) ferritic structure of the steel. Additionally, Si-steels are produced at relatively low manufacturing costs by rolling sheets which are then stacked and layered to assemble full transformer cores [7], [15]. Texturing the Si steel by rolling sheets aligns the easy magnetization directions together and minimizes any detrimental magnetocrystalline anisotropy, or preferred directional magnetization, effects in the resulting transformer core. The anisotropy of the magnetic properties of Si-steels is minimized further by the high symmetry of the B2 ordered BCC structure of the Si-steels. The moderate resistivity of the material is attributed to the substitutional alloying of Si in Fe which increases impurity scattering compared to pure Fe. Fe is an excellent ferromagnetic element and the ferritic BCC structure of Fe has one of the highest J_s of any pure metal known. Low additions of Si to Fe stabilizes a B2 ordered BCC ferritic structure, which further improves the magnetic properties of the BCC structure. The spin orbit interactions of nonmagnetic Si with Fe atoms can cause a slight reduction in the magnetic moment of the bulk alloy, but in low enough concentrations has negligible effects on the measured properties compared to the ferromagnetically ordered structure and crystallographic texture of the alloy [9]. Ultimately, the textured microstructures and B2 ordered BCC crystal structures of Si-steels have enabled their dominance over the transformer core market.

While Si-steels have been the main material used as soft magnetic transformer cores, significant energetic losses in power grids are associated with Si-steels and continue to grow with the global demand for energy. While Si-steels have a relatively high J_s and relatively low to moderate electrical resistivity, other soft magnetic materials can achieve higher individual J_s or electrical resistivity, replacing the alloy in specific applications. Ultimately, a soft magnetic material with a high combination of both J_s and electrical resistivity is needed to improve the resiliency, efficiency, and sustainability of power grids around the world. Recent attempts to outperform Si-steels have included exploration of soft magnetic materials with exotic microstructures and architectures, such as bulk metallic glasses, metal-amorphous nanocomposites, and soft magnetic composites. It has become clear that the long sought-after combination of high J_s and electrical resistivity is elusive as depicted in Figure 2 and the targeted properties are dictated by the designed microstructure of the final material [6], [8], [11], [16]–[18].

Through the investigation of alternatives to Si-steels, the CoFe alloy, also discovered in the early 1900s, has stood out as one of the most promising soft magnetic material systems [19]. The near-equiatomic CoFe alloy has the highest reported J_s of any soft magnetic material at 2.4 T. The highest reported J_s values of the CoFe alloy are attributed to the B2 ordered BCC ferritic structure of the alloy. Between 24 and 90 wt. % Fe in Co, below 700°C, the alloy undergoes a B2 ordering transformation, as depicted in the phase diagram in Figure 3 below from Ohnuma et al [20], [21].

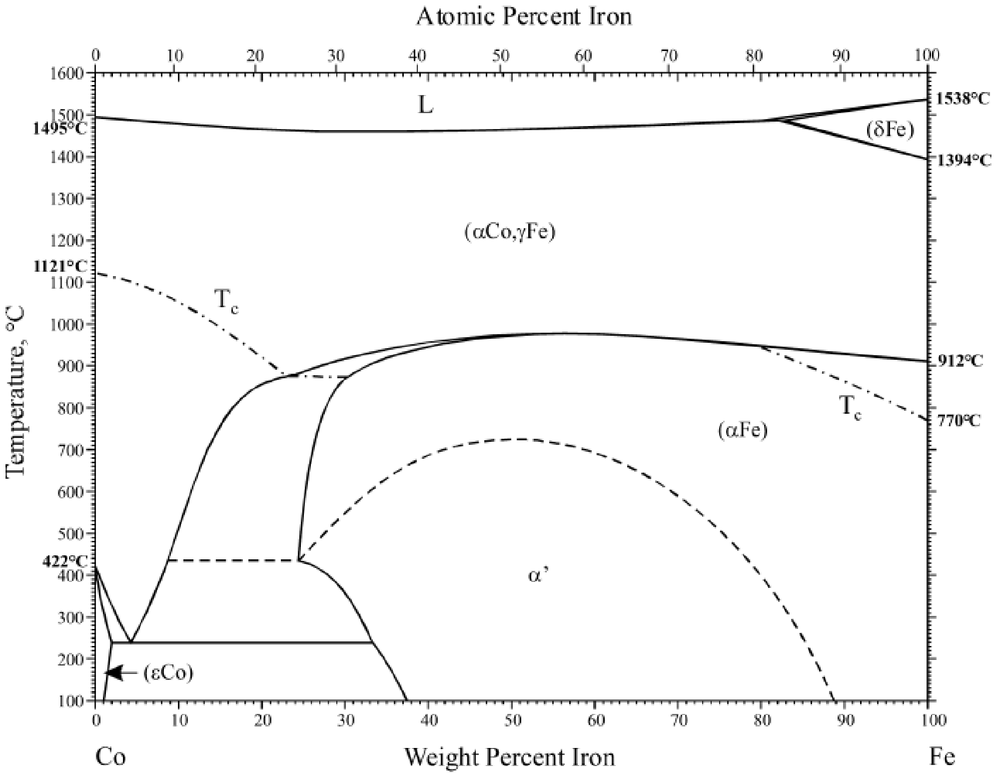

Figure 3. Co – Fe phase diagram reprinted from Ohnuma et al., showing the transformation to the B2 ordered body centered cubic CoFe phase below 700°C, denoted by α' [20].

Due to its extremely high J_s, the near-equiatomic CoFe alloy is one of the most promising candidates to develop more efficient soft magnetic materials. However, due to the metallic nature of the alloy, the CoFe alloy has a low resistivity of approximately 0.1 μΩ·m, [21], [22]. Furthermore, the CoFe alloy is extremely hard and brittle, making it difficult to produce with conventional manufacturing processes and is relatively expensive due to the high price of elemental Co, compared to Fe and Si in Si-steels [15], [23], [24]. Similar to Si-steels, the CoFe alloy must have a strong balance of J_s, electrical resistivity, and ductility to enable its production and use in the transformer core market. The low resistivity, poor manufacturability, of the CoFe alloy, and high cost of Co has prevented the alloy from garnering any widespread use. To accommodate this, in previous studies, V was added to the near-equiatomic alloy to increase the material's ductility [22]. The CoFeV ternary alloy is known as Hiperco and its properties are shown in Figure 2, labeled as Hiperco50 [15], [22]. Further improvements targeting ductility and electrical resistivity of the alloy, have resulted in the development of bulk, nanocrystalline CoFe alloys. Nanocrystalline grains and increased volumes of grain boundaries can increase charge carrier scattering thereby increasing electrical resistivity and also increase strength and ductility of metal alloys [25]–[28]. In other previous literature, soft magnetic composites have been explored through the addition of an insulating secondary phase intersecting a ferromagnetic phase to produce a material with high J_s and high electrical resistivity [29]–[31]. The microstructures of these materials are often produced and controlled by coating ferromagnetic powders, such as Fe, with an insulative coating and then consolidating the coated powder into a bulk composite. As of yet, significant increases to the electrical resistivity of soft magnetic materials have not been realized without subsequent drastic decreases to the J_s of the materials. The relationships between microstructural features and the targeted soft magnetic properties of CoFe - based transformer core materials are summarized in Table 1 below.

Table 1. Summary of the relationships between targeted soft magnetic properties of CoFe – based transformer core materials and suggested microstructural design features.

Property	Microstructural features
High J_s	• Single phase ordered BCC B2 structure • Low concentrations of solute elements in solution • Low volume fraction of voids and secondary phases
High ρ	• High concentrations of solute elements in solution • High volume of defects (e.g., point defects, dislocations, and voids) • Fine grain size • Insulating secondary phases
Low H_c	• Crystallographic texture aligned along the easy magnetization direction • Low volume of defects (e.g. point defects, dislocations, and voids) • Coarse grain size • Low volume fraction of secondary phases

The near-equiatomic CoFe alloy is an extremely promising starting composition in the search of both high J_s and electrical resistivity in a soft magnetic material but further microstructural materials design approaches are necessary for improved efficiency of CoFe – based soft magnetic transformer core materials. Recently, the challenge of the field is to achieve a metallic material with a complex combination of the microstructural features and chemistry necessary for improved soft magnetic transformer cores.

1.4. Research objectives: Designing CoFe – based materials for transformer core applications

Using microstructural design approaches to CoFe – based alloys research aims to design, fabricate, and characterize soft magnetic materials for improved efficiency of transformers. Starting from near-equiatomic CoFe, microstructures in CoFe – based alloys were targeted using non-equilibrium powder metallurgical processing techniques to achieve high electrical resistivity above 1.0 μΩ·m while maintaining extremely high J_s, above 2.0 T. In this research, three powder metallurgical approaches to the microstructural design of CoFe alloys were explored. In the first study, a CoFe – P alloy with an unstable nanocrystalline, solid solution microstructure, motivated by microstructures of deposited films, was targeted to increase the resistivity of the CoFe alloy, while minimizing decreases to the alloy's J_s. To target nanocrystalline solid solutions in these bulk alloys, mechanical alloying and spark plasma sintering processes were used, but a stable intermetallic, detrimental to magnetic properties, was unavoidable. In the second study, to address the poor manufacturability of the CoFe alloy, laser engineered net shaping (LENS®) additive manufacturing was explored as a viable one step processing route. By tuning specific additive manufacturing processing parameters such as laser scan speed, power, and directions, the microstructures of CoFe alloys can be controlled with the potential of unlocking the most efficient magnetic properties of the CoFe alloy. Lastly, in the third study, an inorganic soft magnetic composite, consisting of a non-magnetic, insulative Al_2O_3 phase and soft magnetic CoFe phase, was produced to achieve a high J_s and high electrical resistivity in a bulk alloy. In a proprietary deposition process, CoFe powders were coated with Al_2O_3 and were subsequently consolidated using spark plasma sintering to produce bulk soft magnetic composites. This thesis encompasses three design approaches to more efficient soft magnetic transformer core materials. In all three approaches, the near-equiatomic CoFe alloy was the starting composition and processing – structure – property relationships were utilized to target more efficient magnetic and electronic properties of bulk soft magnetic materials.

Chapter 2: Phase stability in non-equilibrium processed CoFe – P soft magnetic alloys

2.1. Background

In the search for improved performance of soft magnetic transformer core materials, CoFe – based alloys with low solute additions have been successfully designed to target specific mechanical properties without compromising the functional properties of the base CoFe alloy. In the case of the Hiperco alloy, 2 wt. % V (2.2 at. % V) was added to CoFe to increase ductility of the BCC phase without drastically altering the soft magnetic properties of the CoFe alloy. Similar to the case of Si in Fe, the addition of V to the CoFe BCC structure, maintained an extremely high J_s of approximately 2.3 T in the Hiperco alloy. However, the relatively low resistivity of the Hiperco alloy, as in CoFe, prevented widespread implementation as a commercial transformer core material. Nonetheless, compared to CoFe, the Hiperco alloy achieved improved strength and ductility while retaining the CoFe alloy's exceptional soft magnetic properties [22], [25]. By adding only one non-magnetic alloying element in low concentrations to the initial CoFe alloy, the BCC CoFe structure remained stable and detrimental effects to the magnetic behavior of the final alloy were minimized [9]. As discussed previously, the addition of several solute elements to the CoFe alloy, especially in high concentrations can disrupt the BCC phase stability and magnetic behavior of the final alloy, which results in poor soft magnetic performance. Nevertheless, CoFe – based alloy can be designed with low additions of a solute element to target a specific structure and set of combined properties for improved efficiency in soft magnetic transformer core materials.

By examining research of other soft magnetic applications, other prospective alloying elements can be identified. While transformer cores rely on bulk soft magnetic alloys, memory devices, such as hard drives, rely on soft magnetic films with similar properties: high J_s and high electrical resistivity. The design of soft magnetic films can help drive bulk, soft magnetic alloy design for transformers due to their similar targeted properties. In previous literature solid solution, nanocrystalline CoFe – P soft magnetic films were designed for memory device applications. The films developed by Kalu in 2007 and Taslimi et al. in 2015 showed P alloying of up to 6 at. % in $Co_{2.33}Fe$ (Co – 30 at. % Fe) improved the resistivity of the $Co_{70}Fe_{30}$ alloy to nearly 1.0 μΩ·m. The ternary alloy films with up to 6 at. % P also had a J_s up to 1.6 T compared to the $Co_{2.33}Fe$ alloy's 0.94 T [32], [33]. Both the relatively high J_s and high resistivity of the CoFe – P films are attributed to their nanocrystalline, supersaturated solid solution microstructures produced using non-equilibrium film deposition techniques. The resistivity is enhanced by increased charge carrier scattering due to grain boundaries and impurities in a solid solution, which are increased with smaller grain sizes and substitutionally alloyed P in the BCC crystal lattice of CoFe, respectively. In general, the resistivity of solid solution alloys can increase linearly with solute concentration, suggesting the electrical resistivity of the alloy can be increased with higher concentrations of P in CoFe, however the equilibrium solubility limit of P in CoFe is not reported [34]. The J_s was initially increased by the addition of substitutionally alloyed P in the BCC CoFe crystal lattice in a solid solution but was also shown to decrease the J_s in high concentrations of P [32]. As discussed previously, high concentrations of solute elements can result in detrimental changes to magnetic properties of the CoFe alloy, but by limiting the concentration of solute P elements, detrimental effects to magnetic properties of the CoFe – P alloys are minimized [9]. The functional properties of CoFe – P films achieve closer to the ideal combination of magnetic and electronic properties needed in the CoFe alloy and are attributed to the nanocrystalline, solid solution microstructures of the CoFe – P films. By translating the microstructures of CoFe – P films to a large-scale CoFe – P alloy, a more efficient soft magnetic transformer core material can be achieved.

The nanocrystalline, supersaturated solid solution phase of CoFe – P films from previous literature are achieved by non-equilibrium film electrodeposition techniques [32], [33]. At room temperature in thermodynamic equilibrium, P has effectively no solubility in Co and only approximately 5 at. % P is soluble in BCC Fe at 1000°C, with even lower solubility at intermediate temperatures [20], [35]. The solid solution BCC structure achieved by sputtering and film deposition is most likely a metastable solid solution, super saturated with P. Additionally, nanocrystalline grains are thermodynamically unstable and will grow under equilibrium conditions. These super saturated, nanocrystalline microstructures are relatively unstable, but can be produced as films using non-equilibrium deposition processes, as shown by Kalu et al. and Taslimi et al. [32], [33]. These films have ideal magnetic and electronic properties for transformer cores but are on the range of hundreds of nanometers to micrometers thick. Transformer core materials must be a bulk material, typically on a volumetric scale of several cubic millimeters or even cubic meters. Scalable, non-equilibrium bulk processes are necessary to develop CoFe – P alloys with similar metastable microstructures and thus similar J_s and resistivity properties as those in deposited films.

Non-equilibrium powder synthesis and consolidation techniques, such as mechanical alloying and spark plasma sintering (SPS) have the potential to achieve the microstructures necessary for more efficient soft magnetic properties in P containing CoFe alloys with 1:1 ratio by weight of Co and Fe. A mechanical alloying SPEX mill and schematic diagram of the process are shown in Figure 4.

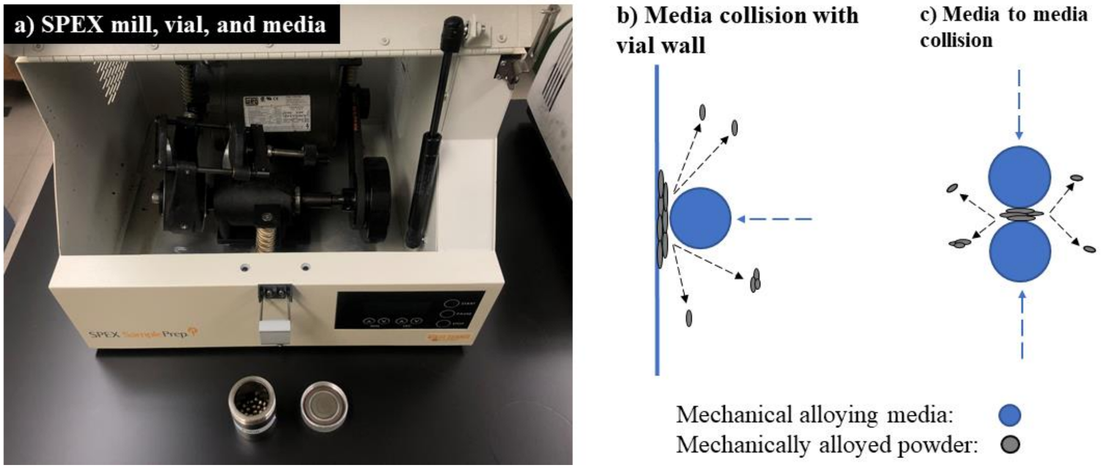

Figure 4. A mechanical alloying (a) SPEX mill, vial, and the media inside the vial, and schematic diagrams of mechanical alloying media collisions with (b) the vial walls and (c) other media causing the severe plastic deformation and eventual mechanical alloying of metal powders.

Mechanical alloying is a non-equilibrium process involving severe plastic deformation of powder particles which yields nanocrystalline, solid solution metal powders. The severe deformation of the mechanical alloying process is produced by high energy collisions, shown in Figures 4 (b) and (c), between the milling media, the milling vial walls, and dissimilar metal powders and produces homogeneously alloyed powders. This severe plastic deformation causes cold welding of dissimilar powder particles and eventual diffusion and mixing at an atomic scale of each constituent. The severe plastic deformation experienced by the powder particles also causes grain refinement, achieving nanometer-scale grains in solid solution alloyed powders. This process can be used to produce unstable super-saturated solid solutions in metallic alloys [36], [37]. However, the severe plastic deformation induced by the colliding milling media can also introduce impurity atoms in the powders, resulting in off composition final powders. From the mechanical alloying media and process control agents, impurity elements such as Fe, C, and O can be introduced into the mechanically alloyed powders. To keep final powder compositions on target, a media with similar composition as the target powders are used. Through mechanical alloying, nanocrystalline, super-saturated solid solution CoFe – P powders can be achieved and by using stainless steel ball bearings as the mechanical alloying media and no process control agent, detrimental impurities can be avoided.

Using non-equilibrium consolidation processes, such as SPS, the microstructures of the powders can be retained in a final, bulk alloy. A SPS apparatus and schematic diagram of the SPS process are shown in Figure 5 (a) and (b) respectively.

Figure 5. A spark plasma sintering (a) apparatus and (b) a schematic diagram of the components, powders, applied current, and applied uniaxial load involved in the process.

SPS is a consolidation process with the capability of sintering powders far more rapidly than conventional sintering [38]. Fundamental explanations of sintering and SPS are beyond the scope of this study, but a brief overview of SPS is provided. During SPS consolidation, loose powders are compacted and concurrently rapidly heated. As shown in the schematic diagram in Figure 5 (b), during SPS graphite dies are used to apply a uniaxial load, compacting the powders. The dies also act as electrodes, applying a pulsed electrical DC current through the powders to reach heating rates on the order of 100°C/min. The pulsed DC current causes Joule heating in the powders being consolidated, especially at the contact points between powder particles, promoting the sintering process and ultimately densification [25], [39]. The high heating rates and rapid densification times characteristic of SPS minimize equilibrium grain growth and can avoid stable phase formation [25], [39]. Because the SPS process still requires relatively high sintering temperatures to reach full densification in metal alloys, consolidating super saturated powders can result in the formation of stable, equilibrium phases, especially in nanocrystalline powders with high volumes of grain boundaries, which serve as preferential nucleation sites for secondary phases. High heating rates and short sintering dwell times can be used when consolidating nanocrystalline, super saturated CoFe – P powders to avoid equilibrium structures. It is possible SPS consolidation may be able to retain the unstable microstructures and solid solutions formed in mechanically alloyed CoFe – P powders. In fact, mechanical alloying and SPS processes have been used to produce metal alloys with nanocrystalline, solid solution microstructures for a range of various applications [25], [39]. Previously, mechanical alloying and SPS have been used to produce bulk nanocrystalline, solid solution CoFe and CoFeV alloys for improved mechanical and functional properties [25], [26], [40]–[43]. Ultimately, CoFe – P alloys with metastable microstructures, necessary for efficient soft magnetic properties, may be attainable using non-equilibrium mechanical alloying and SPS consolidation processes.

In this study, non-equilibrium powder metallurgical approaches were utilized to produce bulk samples of CoFe – P alloys. The phase evolution during processing is investigated and the resulting microstructure’s effect on the functional properties is discussed. CoFe – P alloys with more efficient combinations of soft magnetic properties were targeted via nanocrystalline, super saturated solid solution microstructures in the alloys by using mechanical alloying and SPS consolidation techniques. Mechanical alloying was used to produce nanocrystalline, solid solution CoFe – P powders. The mechanical alloying process may introduce impurity atoms during the induced severe plastic deformation but was avoided by using stainless steel milling media. In the CoFe – P alloy, the nanocrystalline, solid solution microstructure was targeted to increase charge carrier scattering to increase the bulk resistivity of the material. The 1:1 ratio by weight CoFe alloy was used as the starting composition for its high J_s and P was added in low concentrations, minimizing detrimental effect on the J_s of the final bulk alloy as shown in previous literature on CoFe – P films [32], [33]. The P was added to CoFe in a low (0.8 wt. % P) and high (6 wt. % P) concentration targeting a solid solution during mechanical alloying and SPS consolidation. The phase evolution of the alloys during mechanical alloying and SPS consolidation is investigated and discussed with respect to the magnetic and electronic properties of the alloys.

2.2. Experimental methods

2.2.1. Materials preparation

To mechanically alloy the CoFe – P alloy powders, high purity elemental Co, elemental Fe, and Fe_3P powders were used as the starting feedstock powders. The 99.99 % purity powders were purchased from Alfa Aesar (Ward Hill, MA, USA). Three alloy compositions were mixed using the feedstock powders: CoFe, CoFe – 0.8 wt. % P, and CoFe – 6 wt. % P, and will be referred to as such through the rest of this study. For each composition, a Co:Fe ratio of 1:1 by weight was maintained. The high energy SPEX SamplePrep ball mill (SPEX Sample Prep, Metuchen, NJ, USA) shown in Figure 4 (a) was used to mechanically alloy the mixed powders. To avoid introduction of impurity atoms to the CoFe – P powders, Fe-based stainless steel ball bearings were used as the milling media and the powders were mechanically alloyed at room temperature in an Ar atmosphere. As done previously by Dupuy et al., a ball to powder weight ratio of 5:1 (50g of 6.35 mm ball bearings, 10 g of mixed powders) was used to alloy the powders [25]. To prevent the powders from agglomerating or reaching high temperatures, the powders were mechanically alloyed for 20 minutes at a time, with 5-minute rests in between. Two batches of powders were prepared by mechanically alloying for 8 – and 18 – hours. The powders were then consolidated using a Fuji SPS-825S DR. SINTER (Fuji Electronic Industrial Co., Ltd., Kawasaki, Japan), shown in Figure 5 (a), with a maximum pulsed DC output of 12 V and 8000 A under vacuum less than 5 Pa. The uniaxial load was kept under 150 MPa. Each powder composition was consolidated at 700°C with a dwell time of 2 minutes and a heating rate of 60°C/min. The SPS consolidation parameters were driven by previous work on a similar alloy composition using the same SPS equipment [25]. The mechanically alloyed CoFe – 6 wt. % P powders were also consolidated at temperatures of 600°C and 500°C after the formation of an intermetallic phase was observed following consolidation of the powders at 700°C. The final sintered discs measured Φ 5 mm OD x 2 mm HT and were prepared for microstructural and functional properties characterization via metallographic polishing techniques.

2.2.2. Microstructural characterization

The sintered discs were cross sectioned and polished for microstructural and phase composition analysis to validate a nanocrystalline, single phase was retained after sintering. A Rigaku SmartLab X-ray diffractometer (XRD) equipped with a Cu K_α ($\lambda = 0.1542$ nm) radiation source was used to assess phase composition in the mechanically alloyed powders as well as the sintered discs. Each XRD pattern was performed from 20° to 100° with a step size of 0.02° and speed of 2 steps per second. Each pattern was normalized for comparison. From the XRD patterns, the lattice parameter of the mechanically alloyed powders was calculated by the Nelson-Riley Method [44]. The lattice parameters were calculated with accuracy to ten thousandths of an Angstrom (Å), or the 4th decimal place, constrained by the significant figures provided by XRD. The crystallite sizes in the powders were calculated using the Scherrer Formula [45]. Analysis of the surface morphology of the mechanically alloyed powders and cross sectioned sintered discs was performed using a FEI Quanta 3D field emission gun scanning electron microscope (SEM) equipped with a pole piece mounted backscatter electron (BSE) detector, an Everhart-Thornley secondary electron (SE) detector and an Oxford energy dispersive X-Ray spectrometer (EDS). For all bulk samples, the micrographs are normal to the SPS loading direction.

The density of the consolidated samples was measured using the Archimedes method, and compared to the alloys' theoretical densities. The theoretical density of each alloy was calculated by assuming a solid solution of Co, Fe, and P with corresponding atomic fractions in a BCC crystal lattice. The theoretical BCC lattice was assumed to have a lattice parameter of 2.8506 Å, as reported for the B2 ordered BCC structure of CoFe in previous literature [21], [46], [47]. Using the calculated theoretical densities, a relative density was then calculated for each consolidated sample.

2.2.3. Magnetic and electronic properties measurements

To measure the magnetic properties of the sintered discs, a Quantum Design Magnetic Property Measurement System (MPMS) superconducting quantum interference device magnetometer was used. To measure electrical resistivity across the surface of the consolidated discs, four tungsten probes were aligned with 1 mm pitch across the circular face of the discs. To measure resistivity through the height of the consolidated discs, copper strips were fitted to the circular faces of the discs and instead of probes, clips attached to the copper strips were used as the leads. The leads were driven by a Keithley 2425 SMU set to 1 µV resolution and 10 NPLC averaging cycles to reduce noise. The current was swept from 100 mA to 1 A. All discs were isolated from the sample chuck using non-conductive, double-sided tape during measurements.

The magnetic and electronic properties were measured by collaborators at Sandia National Laboratories (SNL).

2.3. Results

2.3.1. Mechanical alloying of feedstock powders

Prior to mechanical alloying and consolidation, the starting feedstock powders were characterized to assess the initial powder size, morphology and phase constitution. Figures 6 (a), (b), (c), and (d) below show the initial feedstock elemental Co, elemental Fe, and Fe_3P powders before mechanical alloying, respectively, and the XRD patterns of the feedstock powders are shown in Figure 6 (e).

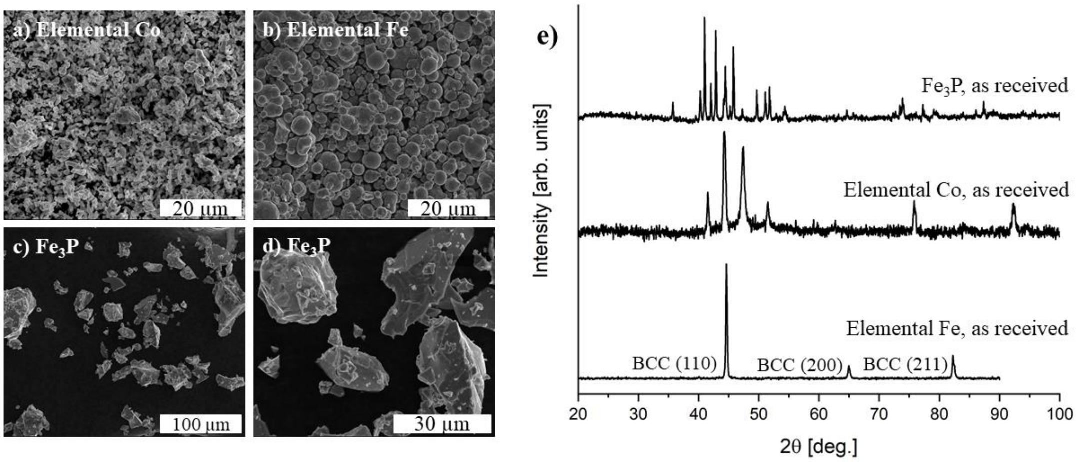

Figure 6. Secondary electron micrographs of feedstock (a) elemental Co, (b) elemental Fe, and (c) and (d) Fe_3P powders and their corresponding (e) X-ray diffraction patterns.

Elemental Co, in Figure 6 (a), and elemental Fe in Figure 6 (b) have powder particle sizes on the order of 5 µm and the Fe_3P powder particles, in Figure 6 (c) and (d), are on the order of approximately 10 µm. While elemental Fe powder particles are mostly spherical, the elemental Co powders appear more elongated. The intermetallic Fe_3P powders appear more faceted with sharp edges and corners. From the XRD patterns in Figure 6 (e), the elemental Fe powders have a BCC structure which is expected to remain during the mechanical alloying process. The HCP and FCC structures of the elemental Co and tetragonal structures of the Fe_3P powders are expected to dissolve into the BCC structure during mechanical alloying. After mixing the feedstock powders in the correct compositions, they were subsequently mechanically alloyed for 8 and 18 hours.

SE micrographs of the powders after mechanical alloying are shown in Figure 7 (a), (b), (c), and (d) and the XRD patterns of the mechanically alloyed powders are shown in Figure 7 (e).

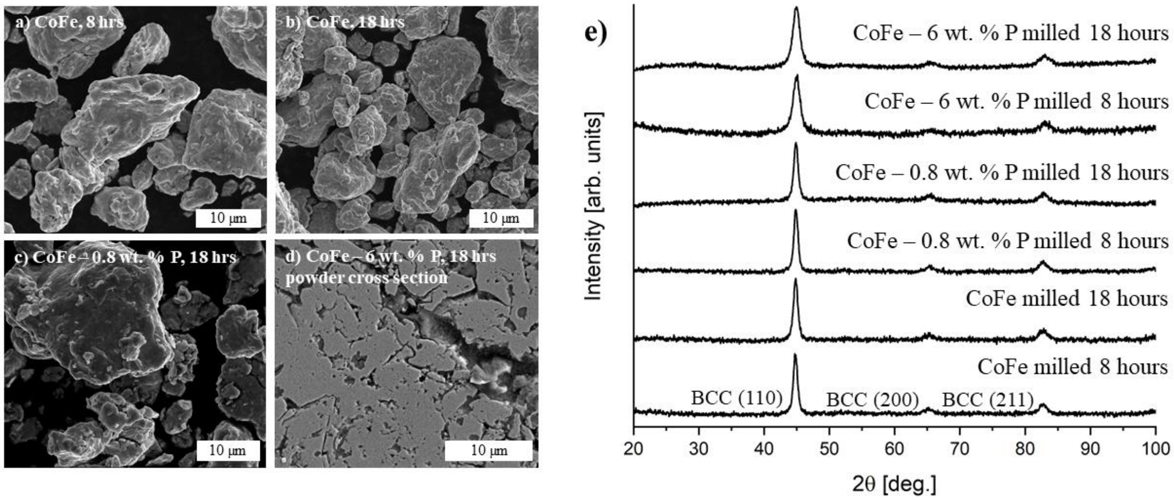

Figure 7. Secondary electron micrographs of the mechanically alloyed (a) CoFe powders after 8 hours of milling, (b) CoFe after 18 hours of milling, (c) CoFe – 0.8 wt. % P after 18 hours of milling, and (d) CoFe – 6 wt. % P, cross sectioned after 18 hours of milling as well as the (e) X-ray diffraction patterns of all powders after 8 and 18 hours of milling.

After both 8 and 18 hours, the mechanically alloyed CoFe powders, in Figure 7 (a), reached average particle sizes of approximately 20 µm. The CoFe – 0.8wt. % P and CoFe – 6wt. % P powders displayed similar morphologies and sizes as the mechanically alloyed CoFe powders, as shown in Figures 7 (a) – (c). In the cross section of the CoFe – 6 wt. % P powders in Figure 7 (d), typical cold welding and fracturing microstructures of mechanically alloyed powders are observed. After mechanically alloying for 8 and 18 hours, the morphologies and sizes of the powders demonstrate the cold welding and fragmentation of the combined feedstock materials necessary to mechanically alloy the powder. Little to no difference in powder morphology and size between the varied mechanical alloying times was observed.

After 8 and 18 hours of mechanical alloying, the powders were characterized using XRD analysis to compare changes in lattice parameter and phase composition across mechanical alloying times and compositions. From the observed peaks in the XRD patterns shown in Figure 7 (e) above, the BCC structure is formed across all mechanical alloying times and in all alloyed compositions. No additional peaks appear in the XRD patterns, suggesting the formation of single phase, solid solution microstructures in the powders. The XRD peaks of the mechanically alloyed powders are increasingly broader with increased P concentration. Increasing shift of the Bragg-satisfying refraction angles is also observed with increasing P content. However, across mechanical alloying times, for each respective alloy composition, little to no peak broadening or shift is observed. After both 8 and 18 hours of mechanical alloying, the powders are well alloyed. The lattice parameters calculated from corresponding XRD patterns are reported in Table 2 below.

Table 2. Extrapolated lattice parameters of the powders mechanically alloyed at various times, calculated from the corresponding X-ray diffraction patterns of the powders.

Powder	Mechanical alloying time [hr]	Extrapolated lattice parameter [Å]
Theoretical CoFe [21], [46], [48]	n.a.	2.8506
CoFe	8 hr	2.9050
	18 hr	2.9031
CoFe – 0.8 wt. % P	8 hr	2.9018
	18 hr	2.8841
CoFe – 6 wt.% P	8 hr	3.1816
	18 hr	3.1851

Compared to the mechanically alloyed CoFe powders, the extrapolated lattice parameter of the CoFe – 6 wt.% P powder is larger by nearly 10 %. For each respective composition of mechanically alloyed powders, less than 0.59 % of change in the lattice parameter was observed between 8 and 18 hours of milling. Little to no additional alloying occurred after 8 hours of mechanical alloying. Not reported in Table 2, from the Scherrer Formula calculations, the crystallite sizes in all the powders after 8 hours reached a minimum of less than 10 nm and underwent less than 10 % change in crystallite size after 18 hours. Powders mechanically alloyed for 8 and 18 hours were both consolidated via SPS since the powders achieved similar nanocrystalline, solid solutions.

2.3.2. Spark plasma sintering mechanically alloyed powders

The XRD patterns of each consolidated sample are presented in Figure 8 below. From the XRD patterns of the consolidated CoFe alloy in Figure 8 below, a solid solution, α-Fe BCC structure in the alloy was maintained during sintering.

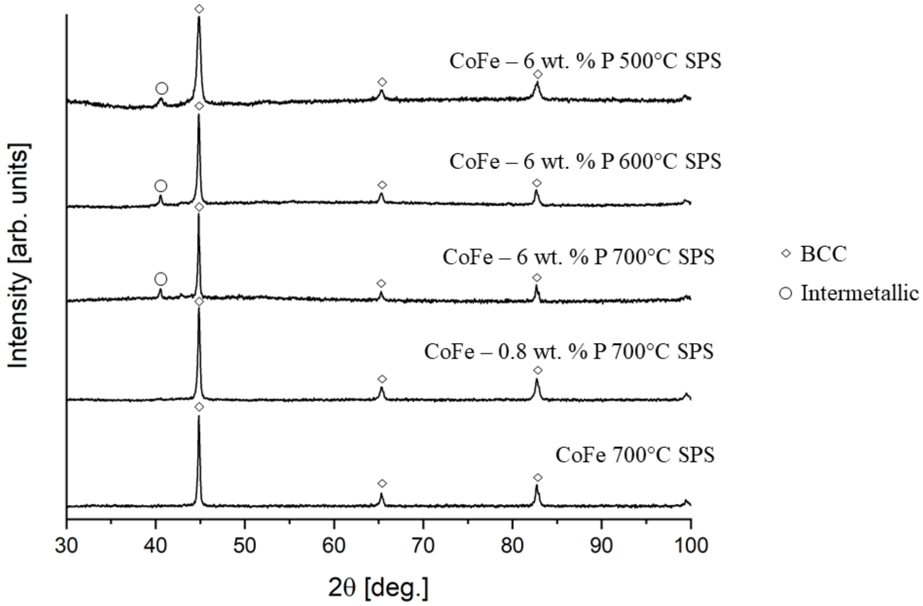

Figure 8. The X-ray diffraction patterns for all consolidated CoFe and CoFe – P alloys, with labeled peaks for the body centered cubic phase, and evidence of secondary phase presence in the CoFe – 6 wt. % P alloy.

From the XRD patterns of the consolidated alloys, and the Scherrer Formula, the grain sizes in the consolidated CoFe and CoFe – 0.8 wt. % P were calculated to be approximately 40 nm. The XRD pattern of the CoFe – 0.8 wt. % P alloy consolidated at 700°C is shown above in Figure 8. From the XRD peak of the consolidated CoFe – 0.8 wt. % P alloy, a solid solution α – Fe BCC structure was maintained with no detectable secondary phase present. No further microstructural analysis was focused on the CoFe – 0.8 wt. % P alloy. Mechanical alloying and SPS consolidation were used to produce a CoFe and a CoFe – 0.8 wt. % P alloy with nanocrystalline, solid solution microstructures. From the XRD pattern of the CoFe – 6 wt. % P alloy consolidated at 700°C, shown in Figure 8 above, in addition to the α-Fe BCC structure, the presence of a secondary phase was detected. The additional phase was indicated by the extra two peaks at 2θ angles of 40.54° and 43.00° in the XRD pattern for CoFe – 6 wt. % P consolidated at 700°C in Figure 8 above. As mentioned previously, the consolidation of the alloys in this study at 700°C was motivated by previous SPS consolidation studies on similar CoFe alloys. Due to the formation of the secondary phase, further CoFe – 6 wt. % P samples were consolidated at lower temperatures of 600°C and 500°C to target solid solution alloys. However, the XRD patterns shown in Figure 8, also contain secondary phase peaks in the alloys consolidated at lower temperatures as well. Using the Scherrer Formula and XRD patterns of the α-BCC phase of the CoFe – 6 wt. % P alloys consolidated at 700°C, 600°C, and 500°C, the grain sizes in the alloys are likely on the order of 50 nm, 20 nm, and 14 nm, respectively. However, it should be noted that the XRD peaks of the secondary phase which precipitated in the CoFe – 6 wt. % P at all three temperatures may likely interfere with and cause broadening of the α-BCC phase XRD peaks. The calculated grain sizes are likely not accurate representations of the actual grain sizes in the consolidated alloys but nonetheless suggest nanocrystallinity in the alloys was maintained. Due to the poor densification of the 600°C and 500°C consolidated samples, further analysis is focused to the 700°C consolidated CoFe – 6 wt. % P alloy.

The consolidated CoFe alloys reached nearly full densification with 98% relative density. SE micrographs of the CoFe and CoFe – 6 wt. % P alloy are shown in Figure 9 (a), (b), (c), (d), (e), (f), (g), and (h).

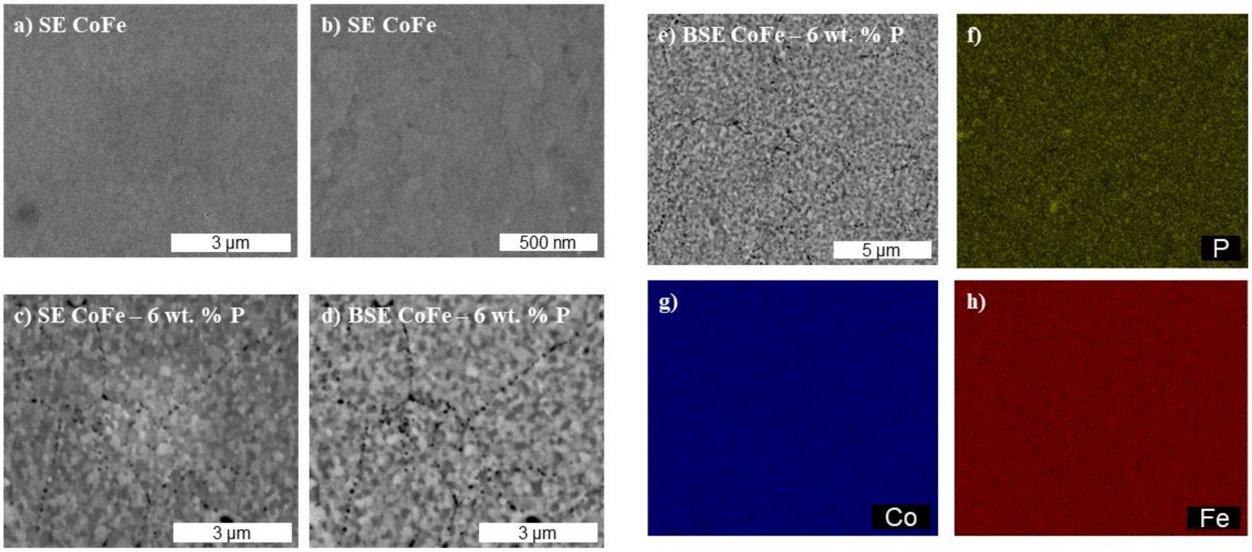

Figure 9. Secondary electron micrographs of the 700°C SPS consolidated CoFe alloy at (a) lower and (b) higher magnifications, showing preferentially polished grain boundaries, (c) SE micrograph and (d) backscatter electron micrograph of the CoFe – 6 wt.% P alloy consolidated at 700°C, showing topological and phase contrast, respectively, and (e) backscatter electron micrograph and (f), (g), and (h) energy dispersive X-ray spectroscopy elemental maps of P, Co, and Fe, respectively in the CoFe – 6 wt.% P alloy consolidated at 700°C, showing localized regions of P enrichment.

From the SE micrographs of the CoFe alloy in Figures 9 (a) and (b), the grain size of the alloy is on the order of 100 – 200 nm. The measured magnetic and electronic properties of the consolidated CoFe alloy are discussed in a later section. A nanocrystalline, solid solution CoFe alloy was achieved using mechanical alloying and SPS consolidation.

The SE micrograph and corresponding BSE micrograph of the CoFe – 6 wt. % P alloy consolidated at 700°C is shown in Figure 9 (c) and (d) above and a BSE micrograph and corresponding EDS elemental maps of the alloy are shown in Figure 9 (e), (f), (g), and (h) above. From the SE micrograph of the 700°C consolidated CoFe – 6 wt. % P alloy, shown in Figure 9 (c), spherical pores can be seen decorating the boundaries between powder particles, but there is little to no porosity in the interiors of the particles. From the contrast in the SE micrograph, due to surface topology, grain sizes on the order of 100 – 200 nm are observed. In the BSE micrograph of the 700°C consolidated CoFe – 6 wt. % P alloy, in Figure 9 (d), four distinct grayscale values can be seen. The darkest features, located at particle boundaries, are nearly black, while the other three are lighter gray values, found within particles and may correspond to grain orientation, surface topology, or secondary phases. As shown in the EDS elemental maps of the 700°C consolidated CoFe – 6 wt. % P alloy in Figures 9 (e) – (h), Fe and Co are well distributed. However, small, nanometer-scale regions of higher P content are seen scattered throughout the sample in Figure 9 (f), and some of the enriched zones of P align with the BSE micrograph of the same area in Figure 9 (e). Both XRD analysis and SEM and EDS microanalysis show evidence of a secondary phase in the CoFe – 6 wt. % P alloy consolidated at 700°C.

2.3.3. Magnetic and electronic properties of consolidated CoFe – P alloys

After consolidating the mechanically alloyed CoFe powders the magnetic and electronic properties of the samples were measured and are reported below in Table 3.

Table 3. Relative densities and measured magnetic and electronic properties as well as secondary phase presence of consolidated CoFe and CoFe – P alloys.

Sample	Relative density (% of theoretical)	Saturation polarization (J_s) [T]	Surface resistivity (ρ) [μΩ·m]	Thru resistivity (ρ) [μΩ·m]	$(Co_xFe_{1-x})_2P$ detected
CoFe 700°C SPS	98.11	2.38 ± 0.02	0.183 ± 0.001	n.a.	n.a.
CoFe – 0.8 wt.% P 700°C SPS	95.21	2.34 ± 0.04	0.105 ± 0.01	.091 ± 0.0005	No
CoFe – 6 wt.% P 700°C SPS	99.03	1.86 ± 0.01	0.17 ± 0.03	0.33 ± 0.12	Yes
CoFe – 6 wt.% P 600°C SPS	97.88 ± 0.16	1.53 ± 0.04	0.89 ± 0.03	0.57 ± 0.12	Yes
CoFe – 6 wt.% P 500°C SPS	88.49 ± 0.24	1.25 ± 0.04	0.208 ± 0.03	2.32 ± 0.12	Yes

As expected, the CoFe alloy had typical J_s and resistivity values of nanocrystalline CoFe. Additionally, not reported in Table 3, the average coercivity of the consolidated CoFe alloy was measured to be approximately 153 A/m. The typical high J_s and low resistivity of the CoFe alloy served to set the baseline for the magnetic and electronic properties of the P containing alloys. Compared with the 1:1 ratio by weight CoFe alloy, little to no significant changes to J_s and electrical resistivity were observed in the 700°C consolidated CoFe – 0.8 wt. % P alloy, as shown in Table 3 above. In the CoFe – 6 wt. % P alloy consolidated at 700°C a dramatic decrease in the magnetic J_s, compared to the CoFe and CoFe – 0.8 wt. % P alloys, was observed. Additionally, the CoFe – 6 wt. % P alloy showed an increase in the electrical resistivity through the bulk of the sample compared to the CoFe and CoFe – 0.8 wt.% P alloys. The coercivity, not reported in Table 3, of the 700°C consolidated CoFe – 6 wt. % P alloy was measured to be on average 4283 A/m.

The 600°C and 500°C consolidated CoFe – 6 wt. % P alloys had progressively lowered relative densities and diminished measured J_s, but progressively increased electrical resistivity.

2.4. Discussion

2.4.1. Mechanically alloyed powders

As the initial feedstock powders were mechanically alloyed, agglomerating, cold – welding, and fracturing, the particle size of the powders progressively decreased as expected [36], [37]. The initial elemental Co and Fe powders had similar sizes and morphologies, but the Fe_3P powders were larger, with faceted morphologies. In general, below 150 µm, the initial powder size and morphology has little effect on the high energy ball milling process [36], [37]. After 8 and 18 hours of milling, the severe plastic deformation of the initial powders caused dissolution of any initial phases and subsequent mixing of atomic elements to achieve a solid solution alloy [25], [26], [36], [37], [43]. The time to reach well-alloyed, α-Fe BCC solid solution structures in the powders was typical of CoFe and other CoFe alloys, [26], [40], [42], [43]. The appreciable changes in lattice parameters calculated from the XRD patterns after 8 and 18 hours of mechanically alloying the powders indicated well-alloyed, solid solution powders were achieved. The broadening of peaks in the XRD patterns shown in Figure 8 is most likely due to lattice strain, nanometer grain sizes, and lattice parameter changes from substitutional alloying, all imparted by the severe plastic deformation process [36], [37]. The slight shift of the XRD peaks with increased P composition was most likely due to substitutionally alloyed P in the CoFe BCC lattice. The atomic radius of P is 55 % larger than that of Fe, and is only 2.5 % smaller than Co. As reported in Table 2, the lattice parameters of the CoFe – 6 wt. % P alloy are much larger than the calculated lattice parameter of the CoFe and CoFe – 0.8 wt. % P alloys. As expected, the incorporation of P in the BCC CoFe lattice increases the lattice parameter of the unit cell, causing XRD peak shift.

The CoFe – 0.8 wt. % P (2 at. % P) may have a low enough concentration of P to have little observed change in the measured lattice parameter of the alloyed powders. While the crystallite size of the powders, calculated to be less than 10 nm, is indicative of nanocrystalline mechanically alloyed powders, the values calculated using the Scherrer Formula are just estimates of the grain sizes in the powders. The Scherrer Formula calculation of crystallite size is dependent on the full width at half the maximum (FWHM) or broadness of the XRD peaks. The broadness of the XRD peaks is not solely affected by grain size, but also the amount of strain in the powders. The Scherrer formula calculations can therefore be complicated and made inaccurate by the large amounts of strain in the mechanically alloyed powders [45]. This calculation of crystallite size can ensure the powders reached the nanocrystalline regime, but further in-depth analysis of the exact grain sizes in the mechanically alloyed powders requires transmission electron microscopy (TEM). Because powders mechanically alloyed for both 8 and 18 hours had well-alloyed, nanocrystalline, solid solution microstructures, they were both used for SPS consolidation. Mechanical alloying was able to achieve nanocrystalline, solid solution and even super saturated microstructures in the CoFe and CoFe – P alloy powders.

2.4.2. Microstructural evolution during consolidation

2.4.2.1. Porosity observed in spark plasma sintered alloys

While very little porosity was observed in the consolidated CoFe alloy, porosity along the boundaries between powder particles was observed in the 700°C consolidated CoFe – 6 wt. % P alloy in Figure 9 (c) and (d). The porosity observed in the 700°C consolidated CoFe – 6 wt. % P alloy is typical and is sometimes observed in mechanically alloyed and SPS consolidated metal powders [49], [50]. From previous literature, the sphericity of the pores suggests the presence of trapped gas. To prevent contamination, the metal powders are mechanically alloyed in Ar gas, and the agglomerating, folding, and welding processes during mechanical milling can trap the Ar gas in the powder particles. The Ar gas trapped in powder particles can possibly move and even become trapped between powder particles during sintering. The porosity along particle boundaries is further observed in the 600°C consolidated CoFe – 6 wt. % P alloy but could potentially be reduced with increased uniaxial load during consolidation. The discrepancy between the amount of observed porosity and the calculated relative density could be due to the formation of a secondary, intermetallic phase and its structure. EDS analysis confirmed no P loss was experienced during milling or consolidation but may not be an accurate assessment of P composition. Porosity in SPS consolidated mechanically alloyed powders is typical and is sometimes unavoidable.

2.4.2.2. Intermetallic phase formation during spark plasma sintering

The formation of a secondary, intermetallic phase was initially observed in the XRD pattern of the 700°C consolidated CoFe – 6 wt. % P alloy in Figure 8. The XRD peaks for the intermetallic phase were not observed in the CoFe – 0.8 wt. % P alloy, suggesting the alloy remained a solid solution after consolidation, or any intermetallic which formed was undetectable. From the XRD peaks at 2θ angles of 40.54° and 43.00° and the processing parameters compared to previous literature, the intermetallic phase is most likely orthorhombic $(Co_xFe_{1-x})_2P$, but a true ternary phase diagram of Co-Fe-P could not be found for comparison [51]–[54].

From the phase diagrams of the Fe-P and Co-P alloys in Figure 10 (a) and (b), reported by Okamoto and Ishida, respectively, orthorhombic M_2P stoichiometries are thermodynamically stable intermetallic structures which may form in both binary systems and potentially at the temperatures and compositions of the consolidated CoFe – 6 wt. % P [35], [55].

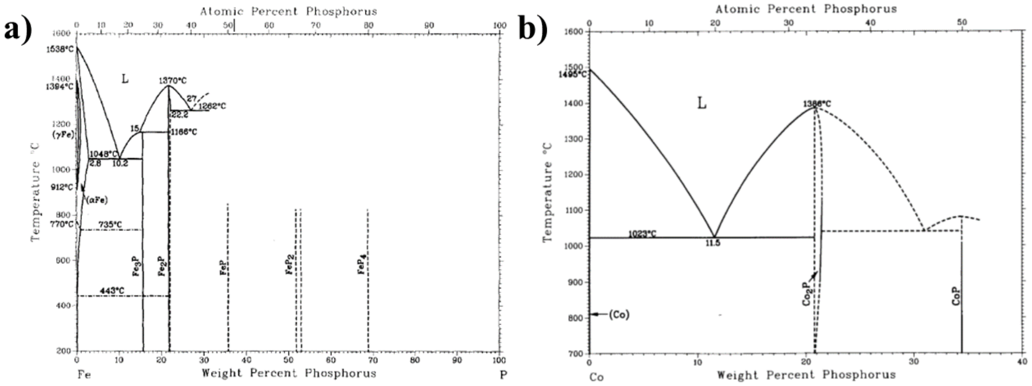

Figure 10. The phase diagrams of the (a) Fe-P and (b) Co-P systems suggest the formation of stable orthorhombic intermetallic structures of the form M_2P reprinted from Okamoto and Ishida, respectively [35], [55].

In the Fe-P system, approximately 2 wt. % P is soluble in Fe, and orthorhombic Fe_2P is a stable intermetallic which can form. In the Co-P system, there is nearly no solubility of P in Co, and orthorhombic or hexagonal Co_2P are stable intermetallic structures which may form. Additionally, by melting Co_2P and Fe_2P together in various ratios, De Vos et al., report a $(CoFe)_2P$ intermetallic is stable for a range of Co and Fe in either an orthorhombic or hexagonal crystal structure [54]. In Figure 9 below, from De Vos, an isopleth phase diagram is shown, wherein the composition of P is held constant, while the ratio of Fe:Co is varied along the x-axis [54].

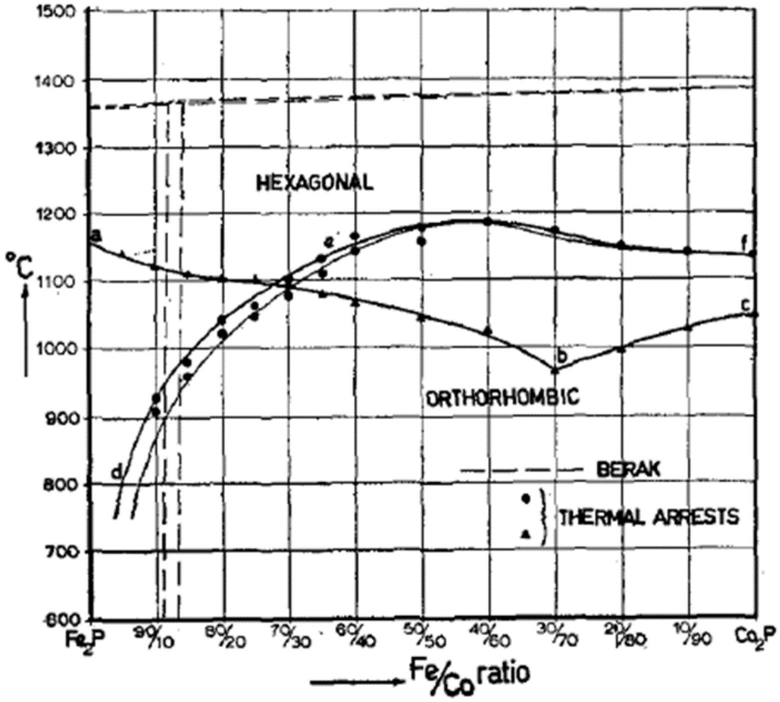

Figure 11. The $(Co_xFe_{1-x})_2P$ phase diagram, reprinted from De Vos et al., suggest a compositional range of Co and Fe in the orthorhombic intermetallic [54].

As shown in Figure 11 from De Vos above, under 900°C, the $(Co_xFe_{1-x})_2P$ intermetallic will exist as an orthorhombic structure. Furthermore, according to Fruchart, the orthorhombic structure of $(Co_xFe_{1-x})_2P$ exists for $x > 0.16$, and any excess Co, Fe, or P will go to a hexagonal form of the intermetallic. The orthorhombic $(Co_xFe_{1-x})_2P$ is the most likely stable intermetallic to form in this alloy based on the composition and sintering temperature of the alloy.

From the XRD pattern in Figure 8, a primary α-Fe BCC phase of Co, Fe, and some solubility of P is present along with the orthorhombic $(Co_xFe_{1-x})_2P$ intermetallic structure. While the solubility of P in CoFe could not be found in previous literature, it is clear that any excess P in solution would be stable in the formation of localized, P rich, intermetallic structures. Based on the XRD peaks in Figure 8, the sintering temperatures used, and the Co and Fe composition of the bulk alloy, it is most likely the orthorhombic structure of the intermetallic is most stable, but any excess Co, Fe, or P not stable in the BCC or orthorhombic phase may have transformed to the hexagonal structure of the $(Co_xFe_{1-x})_2P$ intermetallic, as suggested by De Vos et al and Fruchart [51], [54]. From XRD analysis of the CoFe – 6 wt. % P alloy consolidated at 700°C, the secondary phase which formed is most likely the orthorhombic $(Co_xFe_{1-x})_2P$ intermetallic.

From the P enriched zones observed in the EDS elemental maps and the various grayscale values in the associated BSE micrograph in Figure 9 (c), the $(Co_xFe_{1-x})_2P$ intermetallic phase was observed. First, the darkest, spherical features in the BSE micrographs correspond to the spherical, gas porosity observed in the SE micrographs in Figure 9 (b) and discussed previously. Additionally, the BSE emission coefficients from compositional Z contrast of the α-Fe BCC phase and the intermetallic $(Co_xFe_{1-x})_2P$ were calculated using a method outlined by Lloyd [56]. The BSE emission coefficient of the $(Co_xFe_{1-x})_2P$ intermetallic is only 7.2 % less than the emission coefficient calculated for the BCC CoFe phase. The BSE emission coefficients were calculated for CoFe, with no P in solution, and $(CoFe)_2P$, with equimolar ratio of Co and Fe, so the exact values of the BSE coefficients are not as telling as the comparison between the two. From the minor difference in the calculated BSE emission coefficients, the $(Co_xFe_{1-x})_2P$ intermetallic is expected to only be approximately 7 % darker, backscattering slightly less signal. Based on the calculated emission coefficients, the brightest features in the BSE micrographs in Figure 9 (c) are most likely too bright to all be a distinct, secondary phase, but are instead topologically higher surfaces of preferentially polished grains of different orientations. Some of those grains may even be different orientations of the intermetallic and primary, BCC phase. The two middle, gray tones, observed in the BSE micrograph in Figure 9 (c) then correspond to the BCC CoFe phase and the orthorhombic intermetallic $(Co_xFe_{1-x})_2P$ phase. Additionally, the lighter gray features align with some of the P enriched regions observed in the EDS elemental maps in Figure 9 (c), suggesting the $(Co_xFe_{1-x})_2P$ intermetallic phase is made up of particles in a BCC CoFe matrix on the order of 100-200 nm. Due to the small size of the intermetallic, further in-depth analysis of the crystalline structure of the $(Co_xFe_{1-x})_2P$ intermetallic would require TEM electron diffraction.

In the 600°C and 500°C SPS consolidated CoFe – 6 wt. % P samples, the $(Co_xFe_{1-x})_2P$ intermetallic was again detected in the XRD patterns in Figure 8. The $(Co_xFe_{1-x})_2P$ intermetallic is stable and has a strong, thermodynamic driving force even at temperatures as low as 500°C. The nanocrystalline microstructure of the mechanically alloyed powders, with many sites for nucleation, can further promote the formation of the intermetallic phase. Ultimately, in the CoFe – 6 wt. % P alloy, stable intermetallic formation during SPS consolidation was unavoidable.

Unlike the CoFe – P films discussed previously, in the CoFe – P alloys produced in this study, a stable intermetallic phase was able to precipitate. By comparison, the film deposition techniques used in previous literature are further from equilibrium than the relatively high temperature SPS consolidation process used in this study. To achieve a super saturated solid solution in a CoFe – P bulk alloy, as in the films, lower temperature consolidation processes further from equilibrium are necessary. For example, cold isostatic pressing (CIP) may be able to consolidate mechanically alloyed nanocrystalline, solid solution CoFe – P powders without the need for high temperatures which may cause stable intermetallic phase formation. Ultimately, because the microstructures of the consolidated CoFe – P alloys differ from those of the previously deposited CoFe – P films, the magnetic properties were also expected to differ.

Thermodynamic modeling such as ThermoCalc® Calculated Phase Diagrams (CALPHAD) may be used to study and quantify the thermodynamic stability of the $(Co_xFe_{1-x})_2P$ intermetallic phase and the solubility of P in CoFe. Future studies of this alloy should target a solid solution of P in CoFe, using processes far from equilibrium. Additionally, any ordering of the BCC CoFe and P phase or the orthorhombic $(Co_xFe_{1-x})_2P$ phases was not assessed in this work but should be studied in the future using neutron diffraction or TEM electron diffraction. CoFe – based alloy compositions and should be designed and processed to avoid stable intermetallic structures during consolidation.

2.4.3. Magnetic and electronic behavior

2.4.3.1. CoFe

As has been reported, the exceptionally high J_s of the CoFe alloy is attributed to the B2 ordered BCC structure and thus the atomic neighboring and packing of the CoFe alloy [21], [27], [40], [42], [43]. The nanocrystalline grain size has little effect on the J_s, but can minimize the magnetocrystalline anisotropy of the bulk alloy. The grain size can also affect the hysteresis of the alloy, though not studied in this work [8], [57]. Additionally, to a small degree, the nanocrystalline grain sizes in the microstructure of the CoFe alloy contributed to the bulk electrical resistivity of the material, as grain boundaries are sources of additional charge carrier scattering [34]. Ultimately, the results of the magnetic and electronic properties of the SPS consolidated CoFe alloy in this work are in good agreement with previous literature [21], [25], [26], [43].

2.4.3.2. CoFe – 6 wt. % P

The reduced J_s and especially high coercivity, in all of the CoFe – 6 wt. % P alloys were attributed to the substitutional alloying of P in CoFe, the presence of the nanocrystalline intermetallic phase particles, and porosity in the samples. Additional alloying elements, in this case P, can be detrimental to the magnetic properties of the bulk alloy by minimizing the magnetic ordering strength due to extra electron spins in the alloy lattice [9]. The diamagnetic nature of the P element can have detrimental effects on the ferromagnetic ordering of the BCC CoFe lattice. Additionally, the incorporation of P in the BCC lattice with an atomic radius larger than Fe, can shift the interatomic spacing of the CoFe BCC structure and, by the Bethe-Slater relationship, can disrupt the ferromagnetic ordering of the alloy, decreasing J_s [9]. Beyond the P solubility in CoFe, additional P went into forming a $(Co_xFe_{1-x})_2P$ intermetallic phase, which further diminished the magnetic properties.

Secondary phases can have their own magnetic ordering and strengths, dependent on the structure and composition. While the $(Co_xFe_{1-x})_2P$ intermetallic phase is reported to be ferromagnetically ordered, it was also reported to have hard magnetic properties, characterized by low J_s and high coercivity [54]. The $(Co_xFe_{1-x})_2P$ intermetallic particles were on the order of approximately 100 – 200 nm and could contain several magnetic domains with poor magnetic properties, potentially inhibiting the bulk magnetization of the alloy by affecting the internal fields of the surrounding BCC matrix. Lastly, lack of symmetry, broken bonds, and reduced coordination number associated with the disorder at defects such as grain boundaries and interfaces between dissimilar phases further resulted in the disruption of the magnetization process in the material, minimizing J_s and dramatically increasing coercivity [9].

Similar to the intermetallic phase particles with their own volumes and magnetic properties, pores in the bulk material also had detrimental effects on the measured bulk magnetic properties of the alloy. Pores can impede the movement of magnetic domain boundaries, necessary for magnetization reversal, thus diminishing the measured properties of the material [58], [59]. While the diminished magnetic properties of the 700°C CoFe – 6 wt. % P sample, compared to the CoFe alloy, are mostly attributed to substitutional alloying of P and the presence of the intermetallic phase, subsequent decreases in the 600°C and 500°C consolidated alloy are attributed to the dramatically porous microstructures in the samples. The 600°C consolidated alloy has reduced J_s due to the intermetallic phase presence and increased porosity, compared to the 700°C consolidated sample, as shown by the relative density in Table 3. Furthermore, the 500°C sample which was poorly densified likely had less formation of the intermetallic phase, but large gaps and voids which were observed between particles were most likely attributable to the poor magnetic properties of the sample. In general, structural features on several length scales, as described above, play dramatic roles in designing alloys with targeted magnetic properties. These same structural features and defects can also be attributed to the measured electronic resistivities of the alloys.

In the sintered CoFe – 6 wt. % P alloys, the increased electrical resistivity is attributed to the substitutionally alloyed P in CoFe, the presence of the nanocrystalline intermetallic phase particles, and the porosity of the bulk samples. By Matthiessen's rule, in Equation 2 below,

$$\rho_{Bulk} = \rho_t + \rho_i + \rho_d, \tag{2}$$

the bulk resistivity of a material is the sum of the sources of resistivity in the material [34]. Phonon scattering, ρ_t, the dominant source of electrical resistivity in a material, is intrinsic to the periodic crystalline structure of the material and is temperature dependent. ρ_i is the resistivity due to impurities, and ρ_d is the resistivity due to defects such as grain boundaries and other interfaces. In a metal alloy system, the resistivity due to impurities increases linearly with solute concentration [1], [34]. The substitutionally alloyed P in the CoFe lattice increased resistivity due to impurities increasing the scattering of charge carriers. In the CoFe – 6 wt. % P (10.5 at. % P) alloy, approximately one in every ten atoms in the CoFe structure was replaced by a P atom, disrupting periodic charge carrier motion. The exact contribution to the electrical resistivity of substitutionally alloyed P is difficult to ascertain without a known amount of P in solution in CoFe. Additionally, in this case, any P not in solution was in the $(Co_xFe_{1-x})_2P$ intermetallic. While the bulk electrical resistivity of the $(Co_xFe_{1-x})_2P$ intermetallic could not be found in the literature, according to Matthiessen's rule, the phase contributed to increasing the bulk resistivity of the sintered alloy [34]. Furthermore, the fully enveloped, relatively small intermetallic phase particles may have little effect on the measured electrical resistivity, as the charge carriers may not even interact with the intermetallic phase. The disruption to the periodic crystal structure of the alloy due to disorder at grain boundaries and interfaces between the CoFe matrix and the $(Co_xFe_{1-x})_2P$ intermetallic phase particles on the order of 100 – 200 nm, further contributes to the electrical resistivity of the alloy through defect scattering. The resistivity due to defects, ρ_d, was maximized by achieving a nanocrystalline alloy. On a macro length scale, volume defects such as porosity can have some effect on the electrical resistivity of the bulk alloy. Similar to the intermetallic phase particles discussed previously, the individual pores themselves have little effect on the bulk resistivity of the alloy, as charge carriers can flow through the material without being disrupted by the pores. While pores of various sizes can be detrimental to magnetic properties, as discussed previously, continuous unconsolidated regions between powder particles can dramatically increase resistivity as in the case of the 500°C consolidated CoFe – 6 wt. % P alloy. Not found in the 700°C and 600°C consolidated alloys, large, macro-scale gaps and voids between powder particles found in the 500°C consolidated alloy prevented physical contact between particle surfaces. These voids between particles are attributed to the most dramatic increases in the measured electrical resistivity of the bulk material. Just as structural features and defects are used to target specific magnetic properties in an alloy, those same structures and defects can be used to target electronic properties.

2.5. Summary

Mechanical alloying was used to achieve well-alloyed, nanocrystalline, solid solution CoFe, CoFe – 0.8 wt. % P, and CoFe – 6 wt. % P powders which were then consolidated into bulk alloys using SPS. The bulk 1:1 ratio by weight CoFe alloys showed typical properties and microstructures of nanocrystalline CoFe. The addition of P in the CoFe – 6 wt. % P alloy resulted in some substitutionally alloyed P in a BCC solid solution of CoFe and the formation of a $(Co_xFe_{1-}$

$_x)_2$P intermetallic phase. This intermetallic phase was found to have a strong thermodynamic driving force and precipitated at temperatures as low as 500°C and prevented the achievement of solid solution microstructures observed in CoFe – P films from previous literature [32], [33]. Compared to the 1:1 ratio by weight CoFe alloy, the bulk CoFe – 6 wt. % P alloy displayed poor magnetic properties, however exhibited slightly increased electrical resistivity, attributed to structural features such as P substitution in the CoFe solid solution, the presence of the intermetallic phase, and porosity in the samples. To further target a soft magnetic material with high saturation magnetization and high electrical resistivity, a solid solution alloy is necessary. Further thermodynamic modeling and non-equilibrium processes may be necessary to design an alloy composition to avoid stable secondary intermetallic phases and maintain unstable microstructures. Lower temperature consolidation techniques, such as cold isostatic pressing (CIP), may be necessary to achieve far from equilibrium solid solution structures in bulk alloys from mechanically alloyed powders. Lastly, while a bulk solid solution alloy may be one approach to targeting improved soft magnetic properties, metastable structures such as grain boundary segregants or continuous grain boundary phases may also be key microstructural features necessary for improved soft magnetic properties.

Chapter 3: Influence of an additively manufactured columnar grain microstructure on the magnetic and electronic behavior of the CoFe alloy

3.1. Background

Preferred crystallographic orientations of the grains in polycrystalline soft magnetic materials, can be utilized to tailor the measured magnetic properties of the material. As discussed in Chapter 1, to achieve high J_s and low coercivity in transformer cores, Si-steels are textured by rolling the steel into sheets which are then layered into bulk transformer cores. The rolling process orients grains such that a preferential direction for magnetization is produced along the length of the Si steel sheets and the favorable properties are only measured in the magnetization directions used in the transformer core application [14], [15], [60]. This is possible because crystalline soft magnetic alloys have preferential directions for magnetization which correspond to specific crystallographic directions in the lattice of the alloy. In grain oriented Si-steels, this magnetocrystalline anisotropy is beneficial to the magnetic properties of the alloy since the microstructural texture is controlled, maximizing J_s and minimizing coercivity of the alloy [9]. If the crystallographic texture is uncontrolled, the magnetocrystalline anisotropy of a crystal lattice can be detrimental to the magnetic behavior of a polycrystalline alloy. In a crystal lattice, there are easy and hard directions for magnetization which correspond to soft and hard magnetic properties, respectively. If randomly oriented, the easy and hard magnetization directions of individual grains may cause disruption of the magnetic behavior of a material. It has been previously found that in BCC crystal structures, the easy magnetization direction is along the [100] axis and the hard magnetization direction is along the [111] axis, while the easy direction in an FCC crystal structure is along the [111] axis [9], [10]. Ultimately, spin-orbit-lattice interactions between neighboring atoms and their electrons and crystallographic symmetry dictate the anisotropy of various crystal lattices [9], [61], [62]. Ideally, a textured transformer core material may operate such that the magnetization of the core material is along the easy magnetization direction of the grains of the material. By controlling the crystallographic texture of a soft magnetic material, the efficiency of the material can be improved in specific directions for transformer core applications.

Unlike CoFe alloys, the magnetic behavior of Si-steels has been developed and improved upon for industrial use by texturing the microstructures of the steels. The texturing of grains along the easy magnetization direction in Si-steels is accomplished through the use of conventional rolling processes, enabled by the Si-steel's relatively ductile properties compared to CoFe alloys [14], [15], [60]. By contrast, the polycrystalline equiatomic CoFe alloy with randomly oriented grains has excellent magnetic properties despite the magnetocrystalline anisotropy of the alloy which could be improved by texturing the alloy. However, the CoFe alloy is extremely hard and brittle, preventing the alloy from being manufactured and processed using large scale techniques such as rolling or conventional machining as practiced in Si-steels [21]. To address the manufacturability issues of CoFe alloys, previous studies have focused on developing CoFe alloys with improved mechanical properties, such as development of the CoFeV ternary alloy [22]. A manufacturing technique to process brittle CoFe, while controlling crystallographic texture, is necessary to produce more efficient bulk CoFe alloys at large scales for transformer cores. Additive manufacturing techniques hold potential for producing bulk CoFe alloys with controlled microstructures necessary for more efficient soft magnetic transformer cores.

Additive manufacturing (AM) methods have grown substantially to become potential one-step processes for producing bulk metal components [48], [63]. Metal AM processes, such as laser directed energy deposition (L-DED) rely on the layer-by-layer deposition and solidification of highly localized molten metal [48], [64]. Laser engineered net shaping (LENS®) is a trademarked L-DED technology and has undergone development for use in large-scale industrial applications

[64], [65]. A LENS® apparatus and schematic diagram of the LENS® process are shown in Figure 12 (a) and (b) respectively.

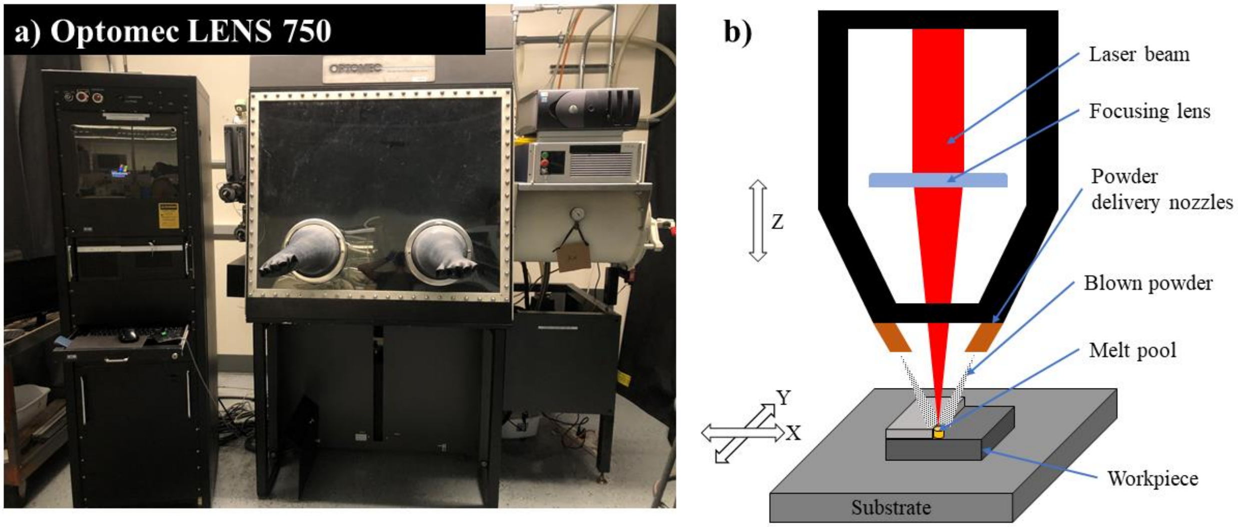

Figure 12. A LENS® (a) apparatus and (b) schematic diagram of the L-DED additive manufacturing process for powder metals.

In LENS® and L-DED processes, as shown in the schematic diagram in Figure 12 (b), blown metal powders are fed to a rastered focal point of a high-power continuous-wave laser beam [66]. The rastered laser produces a melt pool which powder is fed into before solidifying, depositing material on a substrate surface. The layer-by-layer deposition and rapid, non-equilibrium cooling rates on the order of $10^2 – 10^4$ K/s typical of metal AM and L-DED processes such as LENS® produces sharp thermal gradients and complex thermal history in AM components [48], [63], [64]. Adjusting L-DED and LENS® parameters thereby controlling processing conditions has enabled the development of microstructures unique to metal AM processes such as equiaxed, columnar, textured, graded, and even sub-granular cell microstructures in steels, Ti alloys, Al alloys, and Ni alloys [48], [67]–[73]. Development of AM processes has focused on the production of structural alloys to minimize the need for conventional, subtractive manufacturing techniques and have recently turned to the production of functional materials [48], [63], [64]. Because CoFe alloys are so brittle, the use of LENS® and metal AM techniques can potentially be key to producing more efficient transformer cores by eliminating the need for conventional manufacturing of these alloys [48], [67], [68]. The columnar grain microstructures typical of metal AM parts may cause pronounced anisotropic magnetic behavior of the CoFe alloy which can be controlled for more efficient soft magnetic transformer cores.

In this study, the CoFe alloy was deposited using the LENS® process to study the effect of a columnar grain microstructure on the magnetic behavior of the CoFe alloy. The magnetocrystalline anisotropy of CoFe alloys in combination with columnar microstructures common to AM processes can potentially cause improvements to the magnetic behavior of the CoFe alloy in specific directions, enabling development of more efficient transformer cores. If the microstructural texture and thus, magnetic properties, of AM CoFe alloys can be controlled, grain oriented CoFe alloys can be developed to improve efficiency of transformer cores while avoiding conventional manufacturing issues related to brittle CoFe alloys.

3.2. Experimental Methods

Gas atomized, pre-alloyed equiatomic CoFe powder with particle size below 150 µm was purchased from Oryx Advanced Materials (Fremont, CA, USA) and was used as feedstock material for LENS® depositions. The Optomec LENS® 750 Workstation (Albuquerque, NM), shown in Figure 12, fitted with a 1000 W continuous wave IPG Photonics YLR fiber laser with a central wavelength of 1070 nm was used to deposit three 12.7 mm x 12.7 mm x 12.7 mm CoFe sample cubes with the same deposition parameters except laser power. The CoFe samples were deposited in an inert argon atmosphere with less than 20 ppm oxygen concentrations. A powder feed rate of 3 rpm corresponding to 24.2 grams/minute and laser scan speed of 16.9 mm/s were used for all samples with laser powers of 400 W, 450 W, and 500 W. Successive layers were deposited with hatch patterns rotated 90° each layer. The layer thickness was set to 0.38 mm and hatch spacing (spacing between adjacent tracks) was set to 0.25 mm. Using wire electronic discharge machining (EDM), cross sections of the deposited samples were sliced such that the viewing plane was normal to the build direction of the sample. The wire EDM was also used to cut two 5 mm OD x 2 mm HT discs from each deposited sample for magnetic properties measurements. Each sample was cut such that one disc was cut with its cylindrical length parallel to the + Z build direction of the sample, and one disc with cylindrical length perpendicular to the + Z build direction of the sample.

The microstructures of the cross sections of the deposited samples were analyzed using an Olympus BX53 optical microscope after polishing the cross section using 0.4 µm colloidal alumina. All micrographs shown are normal to the + Z build direction of the samples. The densities of the discs cut from the deposited samples were measured using the Archimedes method and a relative density was calculated based on the theoretical density of a BCC CoFe unit cell with lattice parameter of 0.28506 nm, as reported for the B2 ordered BCC structure of CoFe in previous literature [21], [46], [47].

The magnetic and electronic properties of the consolidated discs were measured by a team at Sandia National Laboratories (Albuquerque, NM, USA). The cut discs were used to measure the saturation magnetic polarization and coercivity of the CoFe alloy, perpendicular and parallel to the + Z build direction of the sample using a Quantum Design MPMS superconducting quantum interference device magnetometer. To measure electrical resistivity across the surface of the consolidated discs, four tungsten probes were aligned with 1 mm pitch across the circular face of the discs. To measure resistivity through the height of the consolidated discs, copper strips were fitted to the circular faces of the discs and instead of probes, clips attached to the copper strips were used as the leads. The leads were driven by a Keithley 2425 SMU set to 1 µV resolution and

10 NPLC averaging cycles to reduce noise. The current was swept from 100 mA to 1 A. All discs were isolated from the sample chuck using non-conductive, double-sided tape during measurements.

3.3. Results and discussion

3.3.1. Solidification behavior

In the optical micrographs shown in Figure 13 (a), (b), and (c), columnar grains are observed in the cross sections of as-built microstructures of LENS® deposited CoFe alloys at all three laser power settings.

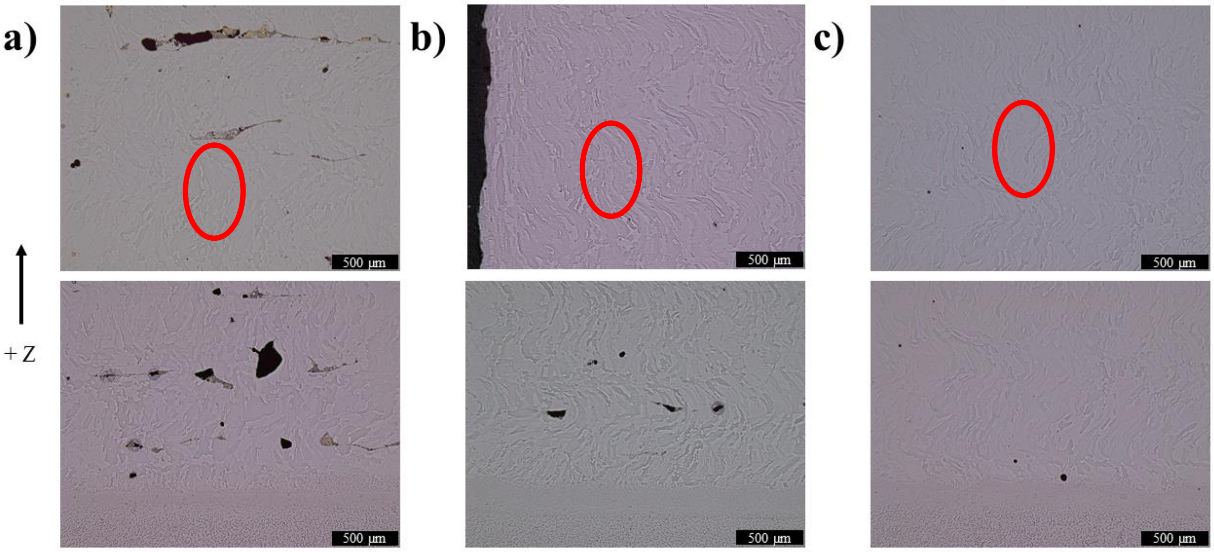

Figure 13. Optical micrographs of the cross section of as-deposited CoFe alloys deposited with laser power settings of (a) 400 W, (b) 450 W, and (c) 500 W, showing columnar grains, circled in red, and spherical and irregularly shaped pores, especially near the substrate-bulk interfaces in the lower micrographs.

The columnar grains observed in all the optical micrographs are on the order of approximately 500 µm tall and approximately 50 – 100 µm wide. The columnar grain microstructure is uniform across the bulk of all the deposited samples. Between samples deposited with the 400 W, 450 W, and 500 W laser power setting, the 400 W deposited sample has the most porosity, the 450 W deposited sample has less, and the 500 W deposited sample has the least amount of observed porosity in

Figure 13 (a), (b), and (c), respectively. Across all the deposited samples, more porosity is observed near the substrate CoFe alloy interface than in the bulk of the CoFe alloy. In the optical micrographs of all the deposited samples, some of the observed pores are spherical. However, in the optical micrographs of the 400 W and 450 W deposited samples, large, irregularly shaped pores are also observed, but are not observed in the 500 W deposited sample. The relative densities of the discs cut from the as-built CoFe alloys are shown in Table 4 below.

Table 4. Measured properties of the discs cut from the as-built CoFe LENS® deposited cubes with varied laser power setting and orientation of discs cut from the sample cubes.

LENS® laser power [W]	Direction of measured properties (ref. to build height, + Z)	Relative density (% of theoretical)	Saturation polarization (J_s) [T]	Coercivity (H_c) [A/m]	Surface resistivity (ρ) [μΩ·m]
400	Parallel to Z	98.21	2.39	338	0.082 ± 0.019
	Perpendicular to Z	97.29	2.41	379	0.08 ± 0.01
450	Parallel to Z	97.41	2.34	332	0.076 ± 0.016
	Perpendicular to Z	98.27	2.38	324	0.087 ± 0.017
500	Parallel to Z	97.73	2.41	325	0.081 ± 0.013
	Perpendicular to Z	97.07	2.36	368	0.075 ± 0.016

As reported in Table 4 above, all the samples were deposited near fully dense, with relative densities above 97%. However, the relative densities reported in Table 4 are measured from the discs cut from the deposited sample cubes and may be misrepresentative. Using the LENS® process, the equiatomic CoFe alloy was well deposited to near full density at laser power settings of 400 W, 450 W, and 500 W.

The columnar grain microstructures observed in Figure 13 (a), (b), and (c) are typical AM microstructures and are approximately ~500 µm tall [48], [74], [75]. In general, the columnar grains are due to the sharp thermal gradients and high heat flow, as reported of LENS® and other metal AM and L-DED processes, and are dependent on the AM process parameters used [48], [63], [74], [75]. The thermal gradients and heat flow during the AM process were not studied in this work but can be quantified from thermal measurements during the build process. These process conditions and thereby the AM process performance and the as-built microstructures, can be controlled by adjusting the AM process parameters, such as scan speed, powder feed rate, laser power, etc. [63], [76], [77]. For example, equiaxed grains in the CoFe alloy can possibly be achieved by increasing solidification rates and reducing thermal gradients which can be attained by slowing scan speeds and using minimal laser power. However, in general, higher laser power is necessary to improve material deposition rate and density [63], [78]. In this study, only optical microscopy was used to observe the microstructures of the as-built CoFe alloys. From previous studies of the LENS® hatch rotation parameter used in this study, there is likely little to no texturing in the CoFe alloys [73]. The rotation of the laser scan direction in subsequent hatched layers randomizes the orientation of solidifying and growing grains. As reported by Terrassa et al., by using a LENS® hatch rotation parameter of 0°, crystallographic orientation is maintained across subsequent deposited layers [73]. In future AM studies of the CoFe alloy, this phenomenon could be useful in developing a textured CoFe alloy. However, it may be noted the bulk dimensional accuracy of an as-deposited part is improved by using cross hatching, instead of overlaying tracks directly atop each other in the same path and direction. Ultimately, the as-built CoFe alloys consisted of columnar grain microstructures, typical of LENS® and metal AM.

The porosity observed in the deposited CoFe alloys is also typical of metal AM microstructures. As expected, in Figure 13 (c), smaller and less frequent pores are observed in the optical micrographs of the 500 W laser power deposited sample, as compared to the 450 W and 400 W laser power deposited samples. As previously reported, the higher laser power increased the energy density applied to the melt pool during the AM process and assisted in increasing material deposition density [63], [77], [78]. The irregularly shaped pores, in Figure 13 (a) and (b), were observed in the optical micrographs of the samples deposited with 400 W and 450 W laser powers. Upon close inspection, particles which were not properly melted are observed in the pores and around the pore edges. Either a higher laser power, slower scan speed, or smaller hatch spacing can be used to fully melt these particles and eliminate these lack-of-fusion pores [63], [78]. The spherical pores seen in all the samples are most likely due to trapped argon gas or could be shrinkage voids formed during the rapid solidification of the deposited material. Additionally, more porosity observed near the substrate – deposited alloy interface is typical of AM processes as parameters are static and do not account for material property changes. Ultimately, the samples of all three laser power settings were well deposited to near full densification and had typical LENS® microstructures.

3.3.2. Magnetic and electronic behavior

As reported in Table 4 above, the J_s and coercivity of all the discs, both perpendicular and parallel to the LENS® build direction was measured to be on the order of 2.3 T and 300 A/m, respectively. The electrical resistivity of the CoFe discs, both perpendicular and parallel to the LENS® build direction was measured to be on the order of approximately 0.08 μΩ·m. The relatively high J_s, low coercivity, and low electrical resistivity measured in the LENS® built CoFe alloy discs were typical properties of CoFe alloys processed with other methods [9], [15], [21].

Additionally, the properties measured parallel and perpendicular to the LENS® build direction show little to no significant dependence on directionality.

Despite the columnar grain microstructure, little to no effect of the columnar grain orientation on magnetic properties was observed. While specific grain orientation may not necessarily drastically diminish or increase J_s, the coercivity can dramatically shift, depending on the alignment of the easy and hard magnetization directions of the crystal structure [9], [21], [61], [62], [79]. However, no such shift in coercivity is observed between properties measured parallel or perpendicular to the columnar grains and LENS® build direction. Despite the columnar grain microstructure extended along the length of the LENS® build direction, the orientation of the columnar grains is still likely random, not textured. Random orientations of grains, columnar or otherwise, diminish the observable effects of the magnetocrystalline anisotropy of the underlying crystal structure of soft magnetic alloys. Furthermore, the B2 ordered BCC structure of the CoFe alloy has high symmetry and can be described by two super-imposed simple cubic crystal structures. The high symmetry of the B2 structure can further diminish first order terms in the calculations of magnetocrystalline anisotropy [9], [21]. In these LENS® deposited alloys, the columnar microstructure had little effect on the magnetic properties of the CoFe alloy because their crystallographic orientations were still random. To truly control the anisotropic nature of the CoFe alloy to improve magnetic properties, further control of texture and discrete grain orientation is necessary. In the future, further characterization of the exact orientations of columnar grains is needed to determine the effects of the microstructure on the anisotropic behavior of LENS® deposited CoFe. Additionally, in this work, high electrical resistivity in the CoFe alloy was not targeted, but as suggested by Goll et al., microstructures achievable with AM, such as intentional pores, voids, or channels can be designed and fabricated to target high resistivity in a bulk CoFe alloy. As discussed previously, adjusting the hatch rotation parameter may be key to controlling the texture of as-deposited CoFe alloys. AM is a key process in further amplifying the design of CoFe alloy compositions and microstructures with targeted properties for more efficient soft magnetic transformer cores and can be further developed with process parameters which control the texture of CoFe alloys in as-built parts.

3.4. Summary

The LENS® AM process was used to deposit the CoFe alloy with columnar grain microstructures. The magnetic properties of the CoFe alloys were as expected and typical of CoFe alloys processed with other methods. Little to no effect of the magnetocrysalline anisotropy of the alloy was observed, despite the columnar grain microstructure. This lack of anisotropy was attributed to the fact that despite the columnar morphology of the grains, the orientations of the grains was random. Texturing of AM deposited grains may be achieved by adjusting the LENS® hatch rotation parameter. AM can be a powerful tool for producing large scale CoFe-based transformer core alloys, especially if process parameters are tuned to control texture of the deposited alloy. Future CoFe alloys for soft magnetic transformer cores should be designed with the forethought of the AM process conditions to enable AM achievable microstructures.

Chapter 4: The influence of an Al_2O_3 coating on consolidated CoFe powder

4.1. Background

Development of soft magnetic composites (SMCs) as a design approach to more efficient soft magnetic transformer cores began in the 1990s and gained notoriety for their potential to significantly minimize magnetic energy losses [8]. SMCs can potentially achieve high J_s, low coercivity, and high electrical resistivity, necessary to maximize power density and minimize magnetic energy losses, when a magnetically ordered phase is properly intermixed with a non-magnetic and electrically insulating phase [8], [29], [30], [80], [81]. From Equation 1, in Chapter 1, by increasing the bulk electrical resistivity and by reducing d, electrical domain size of eddy currents of a soft magnetic material, the eddy current losses of the material are reduced [9]. SMCs can achieve high bulk electrical resistivity and reduced electrical domain sizes by fully intersecting a magnetic phase with a continuous phase which is non-magnetic and electrically insulating. Ultimately, the achievable magnetic properties of a SMC are controlled by the volume fraction, morphology, and distribution, of the non-magnetic, insulating phase. If not properly controlled, a high volume fraction of the non-magnetic phase detrimentally increases coercivity and reduces J_s and permeability by physically separating and inhibiting magnetic interaction between the magnetic phase. Compared to discontinuously distributed non-magnetic fibers or particles, a continuous non-magnetic phase intersecting dispersed particles of a magnetic phase has been shown to be more effective at tailoring the magnetic and electronic properties of SMCs. A continuous phase prevents long range charge carrier transport and more effectively increases the measured resistivity of the SMC. Additionally, the thickness of the continuous phase between magnetic particles can be adjusted to tailor the magnetic interaction of the particles and thus the magnetic behavior of the SMC. The volume fraction, morphology, and distribution of the magnetic phase in an SMC can be adjusted to maintain high J_s, high permeability, and low coercivity, and achieve high electrical resistivity [29], [30], [80], [81]. Development of SMCs and their microstructures can potentially achieve more efficient properties for soft magnetic transformer cores.

One of the most practical approaches to SMC development has been the consolidation of coated ferromagnetic powder particles. Ferromagnetic powders maximize the achievable J_s in SMCs and are coated with an insulating layer to restrict charge carrier movement in the bulk, consolidated SMC. Once consolidated, the coatings on the powder particles form a continuous phase, intersecting the ferromagnetic particles. By selecting powder particle sizes (typically on the range of 5 – 200 µm) and controlling the powder coating thickness, the bulk volumetric phase fraction of the insulating phase can be adjusted [29], [30], [80], [81]. In many studies, Fe powders have been coated with organic polymers such as epoxies and resins, allowing the coated powders to be densified with relatively low consolidation pressures and temperatures. Organic polymer SMCs yielded moderate resistivity, on the order of 100 µΩ·m, but typically do not withstand temperatures above 300°C and have low J_s, less than 1.0 T [82], [83]. In other approaches, consolidated SMCs made with coatings of Al_2O_3 or SiO_2 on Fe powder particles reached high resistivities on the order of 100 - 1000 µΩ·m, and moderate J_s, approximately 1.0 - 1.5 T [84]–[88]. However, the processes used to coat powders with Al_2O_3 are relatively small-scale batches and have not enabled large production volumes of SMCs. Furthermore, the ceramic coating on metal powders requires higher temperatures and thus longer sintering and consolidation times, allowing equilibrium structures to form which may hinder magnetic and electronic properties [30], [80]. Large-scale, powder coating and consolidation processes are necessary to develop more efficient SMCs for transformer core applications. In recent years, deposition methods have been developed to effectively coat large batches of metal powders with ceramic coatings. Industrially developed Al_2O_3 coating deposition processes can produce large volumes of coated powders which can be consolidated into SMCs with controlled microstructures and properties. Non-equilibrium SPS consolidation processes have been developed over the years and can rapidly consolidate metal and ceramic powders. The rapid heating rates and sinter times associated with SPS can be used to fully densify metal powders coated with a ceramic without the formation of new phases or mixing of the constituent elements. Instead of Fe, the equiatomic CoFe alloy which has significantly higher Js can be used as the ferromagnetic powder to maintain better soft magnetic properties in SMCs [21], [30], [80]. In this study, A large-scale deposition process was used to coat a large volume of CoFe powder particles which were subsequently densified using SPS consolidation. A fully dense SMC with an Al_2O_3 phase fully intersecting CoFe powder particles was targeted by consolidating the coated CoFe powders using SPS to achieve high J_s, above 2.0 T, and high electrical resistivity, above 1.0 μΩ·m.

4.2. Experimental methods

4.2.1. Material preparation

Gas atomized, pre-alloyed equiatomic CoFe powder particles, with a particle size below 150 µm, were purchased from Oryx Advanced Materials (Fremont, CA, USA) and were used as the feedstock powder to be coated with Al_2O_3. Approximately 1 kg of CoFe powder particles were coated with 2 vol. % Al_2O_3 by Advanced Powder Solutions (Middlesex, NJ, USA) with a proprietary chemical vapor deposition process. Using a Fuji SPS-825S DR. SINTER (Fuji Electronic Industrial Co., Ltd., Kawasaki, Japan) SPS with a maximum pulsed DC output of 12 V and 8000 A, the as-coated powders were consolidated at 700°C and 1000°C under a vacuum of less than 5 Pa to form 5 mm OD x 2 mm HT samples. The samples were then polished for magnetic properties measurements and cross sectioned for microstructural evaluation.

4.2.2. Microstructural characterization

The Archimedes method was used to measure density of as-consolidated SMC discs. To assess the relative density the measured density was compared to the theoretical density of a BCC CoFe structure with 2 vol. % Al_2O_3. The phase composition of the as-received powders and consolidated SMCs was assessed with a Rigaku SmartLab X-ray diffractometer (XRD) equipped with a Cu K_α (λ = 0.1542 nm) radiation source. As-received coated powders were mounted in KonductoMet™ and mechanically polished to 0.04 µm to evaluate the microstructural features of the cross-sections of powders. The consolidated SMCs were cross-sectioned using wire electronic discharge machining (EDM) and were mechanically polished to 0.04 µm to evaluate the microstructural features in the cross-section of the SMCs, perpendicular to the SPS loading direction. The microstructures of cross-sectioned as-coated powders and consolidated SMCs were characterized using a FEI Quanta 3D field emission gun scanning electron microscope (SEM) equipped with a pole piece mounted backscatter electron (BSE) detector and an Oxford energy dispersive X-Ray spectrometer (EDS). All micrographs of the consolidated discs are normal to the uniaxial SPS loading direction.

4.2.3. Magnetic and electronic properties measurements

The magnetic and electronic properties of the consolidated discs were measured by a team at Sandia National Laboratories (Albuquerque, NM, USA). To evaluate the J_s and coercivity of the consolidated discs, the magnetic properties were measured using a Quantum Design MPMS superconducting quantum interference device magnetometer. To better measure the effects of the Al_2O_3 coating and avoid surface defects from the consolidation and polishing process, the electrical resistivity through the height of the consolidated discs was measured. To measure resistivity through the height of the consolidated discs, copper strips were fitted to the circular faces of the discs and clips attached to the copper strips were used as leads. The leads were driven by a Keithley 2425 SMU set to 1 μV resolution and 10 NPLC averaging cycles to reduce noise. The current was swept from 100 mA to 1 A. All discs were isolated from the sample chuck using non-conductive, double-sided tape during measurements.

4.3. Results

4.3.1. As-coated powder

The SE micrograph and corresponding BSE micrograph and EDS elemental maps of the as-coated powders are shown below in Figure 14 (a), (b), (c), (d), and (e) respectively.

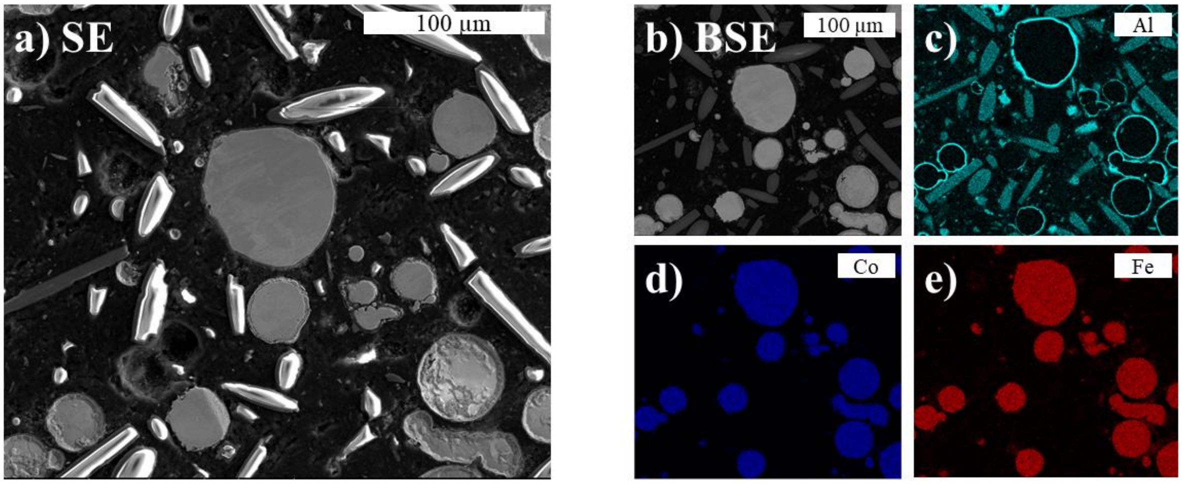

Figure 14. (a) Secondary electron micrograph of as-coated Al_2O_3 coated CoFe powders and (b) corresponding backscatter electron micrograph and energy dispersive X-ray spectroscopy elemental maps depicting the Al_2O_3 coating fully surrounding the CoFe powder particles.

The bright, needle-shaped particles in the SE micrograph in Figure 14 (a) are artifacts of the KonductoMet^{TM} polymer the powders are mounted in for cross-sectional polishing. From the SE micrograph in Figure 14 (a), spherical powder particles with an average particle size on the order of 10 μm are observed. Grain features can be observed in both the SE and BSE micrographs in

Figure 14 (a) and (b) and have grain sizes on the order of 5 µm. In the BSE micrograph in Figure 14 (b), the Al_2O_3 coating is observed as a dark gray phase surrounding powder particles. The Al_2O_3 coating is also observable in the EDS elemental maps in Figure 14 (c) fully coating CoFe powder particles. The Al_2O_3 coating is approximately 2 - 5 µm thick. In Figure 15 below, the XRD pattern of the as-coated powders is plotted and is compared with the SMCs made from the powders, consolidated at 700°C and 1000°C.

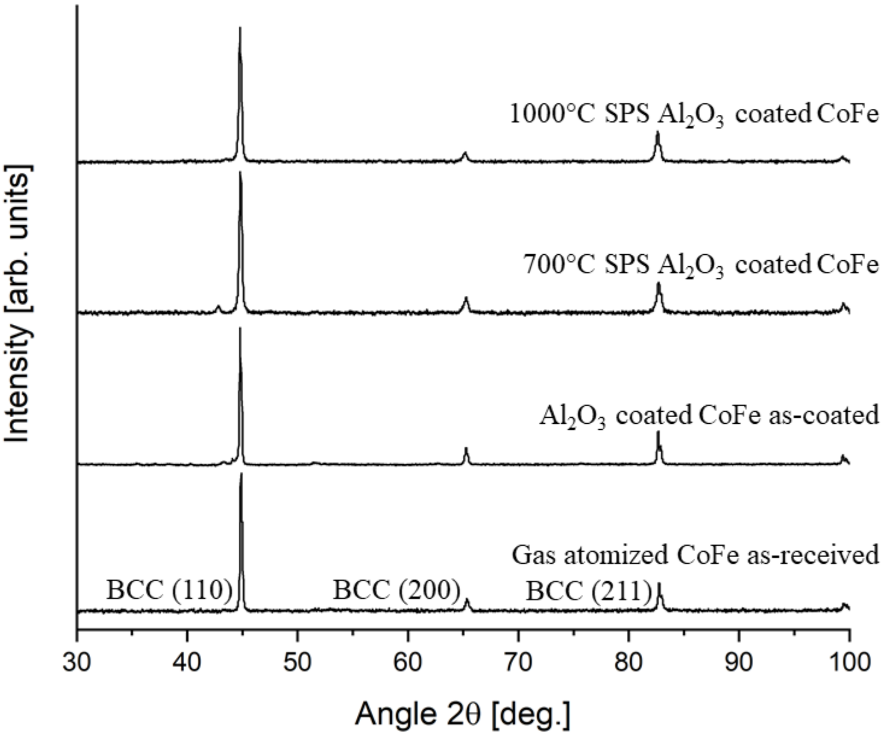

Figure 15. X-ray diffraction patterns comparing the as-received gas atomized CoFe powders, the as-coated Al_2O_3 coated CoFe, and the coated powders consolidated at 700°C and 1000°C.

From the XRD pattern of the as-coated powders in Figure 15, additional Bragg's Law satisfying peaks, corresponding to Al_2O_3 appear at 2θ angles of 40.289° and 44.097° in addition to the major BCC peaks for CoFe. The coated powders were consolidated at 700°C and 1000°C, targeting fully dense SMCs with the Al_2O_3 phase intersecting the CoFe powder particles for high J_s and high electrical resistivity.

4.3.2. Spark plasma sintered CoFe – Al_2O_3 soft magnetic composites

4.3.2.1. 1000°C spark plasma sintered soft magnetic composite

The XRD pattern of the CoFe – Al_2O_3 composite is shown in Figure 15 for comparison with the as-coated powder before SPS consolidation. As shown in the XRD pattern of the 1000°C consolidated composite, after SPS consolidation, the major peaks for a BCC CoFe structure are observed. Unlike the as-coated powder XRD pattern, an additional peak is not observable or indexed by the Rigaku SmartLab XRD software. Similar to the as-coated powder XRD pattern, the observed peaks are relatively narrow. The relative density of the 1000°C consolidated composite is just under 95 %.

The SE micrograph and corresponding BSE micrograph and EDS elemental maps of the cross section of the 1000°C consolidated CoFe – Al_2O_3 composite are included below in Figures 16 (a), (b), (c), (d), and (e) respectively.

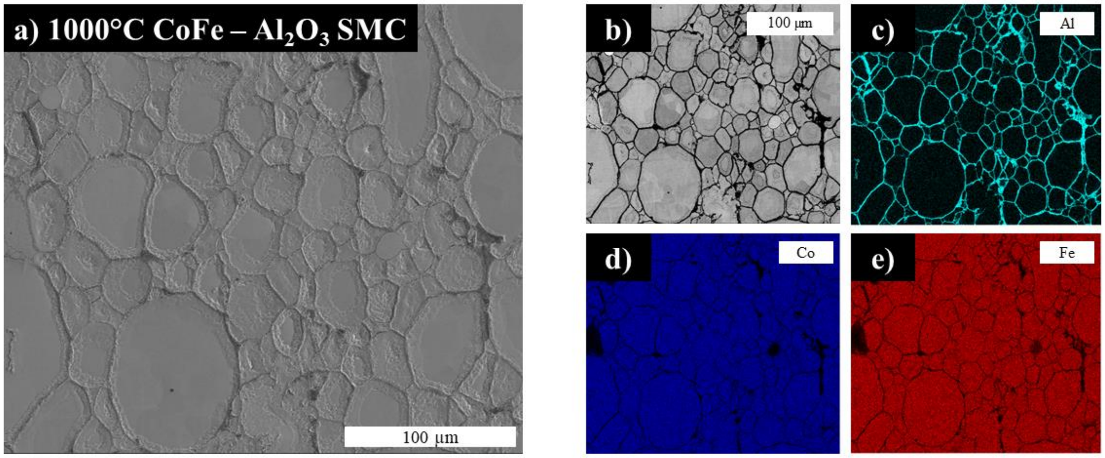

Figure 16. (a) Secondary electron micrograph of 1000°C consolidated CoFe - Al_2O_3 composite and (b) corresponding backscatter electron micrograph and energy dispersive X-ray spectroscopy elemental maps depicting the Al_2O_3 coating fully surrounding the CoFe powder particles.

In the SE and BSE micrographs, little to no porosity is observable between powder particles, but some small, nanometer scale pores are found within powder particles. In the SE micrograph in Figure 16 (a), consolidated powder particles, bounded by the Al_2O_3 coating are observed. The polished Al_2O_3 coating has a morphologically different surface topology from the polished CoFe powder particle cores, observable in the SE micrograph. From the corresponding BSE micrograph and EDS elemental maps in Figures 16 (b), (c), (d), and (e) the Al_2O_3 coating is distinctly observable from the CoFe powder by BSE contrast and EDS element detection. The coating is approximately 1 – 3 µm in thickness. In the BSE micrograph, the Al_2O_3 phase appears nearly black and the CoFe phase appears light to medium gray with contrast within powder particles due to grain orientation. Compared to the as-coated powder particles shown in Figure 14 (a) and (b), the 1000°C consolidated powders appear less spherical and more elongated, and the average particle size remains on the order of 10 µm. Within the 1000°C powder particles, the grains appear to be larger than grains in the as-coated powders and have a grain size of approximately 10 µm, the same order of magnitude as the powder particles themselves. From Figure 16 (a) and (b), it is clear the powder particles consolidated at 1000°C are packed tightly with a near uniform Al_2O_3 phase coating the boundaries between particles.

A SE micrograph and corresponding BSE micrograph of the 1000°C consolidated composite at higher magnification is shown below for further analysis in Figure 17 (a) and (b), respectively.

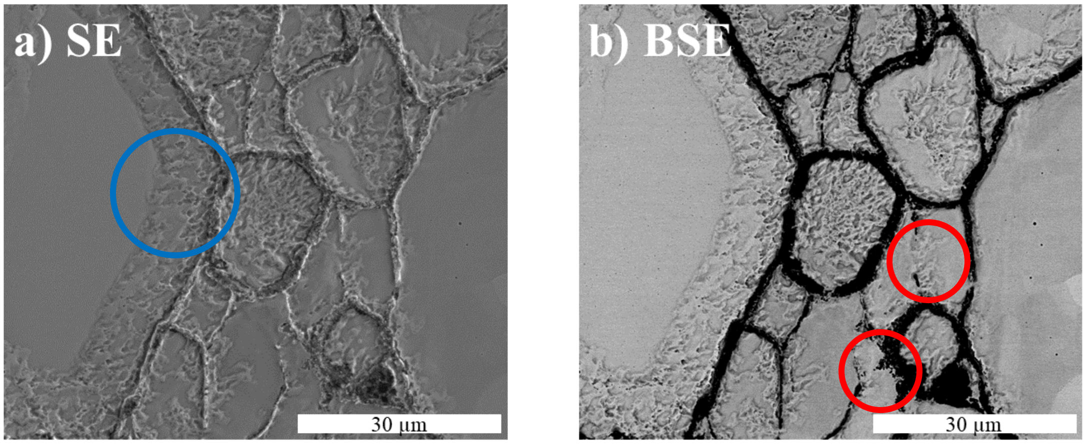

Figure 17. Higher magnification (a) secondary electron micrograph and (b) corresponding backscatter electron micrograph, depicting the morphological barriers found in the particles, circled in blue and regions where CoFe appears between powder particles, in the Al_2O_3 coating regions, circled in red.

Upon closer inspection of the boundaries between consolidated powder particles at high magnification, some CoFe between powder particles, in the Al_2O_3 coating regions, are observed. This CoFe presence in the coating is circled in red in the BSE micrograph in Figure 17 (b) above and can be observed upon close inspection of the EDS element maps in Figures 16 (c), (d), and (e). In the SE micrograph in Figure 17 (a), the Al_2O_3 coating can also be seen broken up in some regions between powder particles. Lastly, in the SE micrograph in Figure 16 (a) and circled in blue in the SE micrograph in Figure 17 (a), a morphological barrier up to approximately 10 µm wide is observed within powder particles, separating the Al_2O_3 coating from the CoFe powder particle core. However, no compositional or grain orientation difference is observed in the barriers in the BSE micrographs or EDS elemental maps.

4.3.2.2. 700°C spark plasma sintered soft magnetic composite

The XRD pattern of the 700°C consolidated SMC are shown with the as-coated powders XRD pattern in Figure 15 above. Like the 1000°C consolidated composite and the as-coated powder XRD patterns, the peaks of the 700°C consolidated composite XRD pattern are relatively narrow and the major peaks for the BCC CoFe phase are observed. In addition to the major BCC peaks, a peak corresponding to Al_2O_3 is observed at a 2θ angle of 42.764°. The additional peak in the 700°C consolidated composite XRD pattern does not appear at the same 2θ angle as the additional peaks in the as-coated powder XRD pattern.

The SE micrograph and corresponding BSE micrograph and EDS elemental maps of the 700°C consolidated composite are shown below in Figure 18 (a) (b), (c), (d), and (e) respectively.

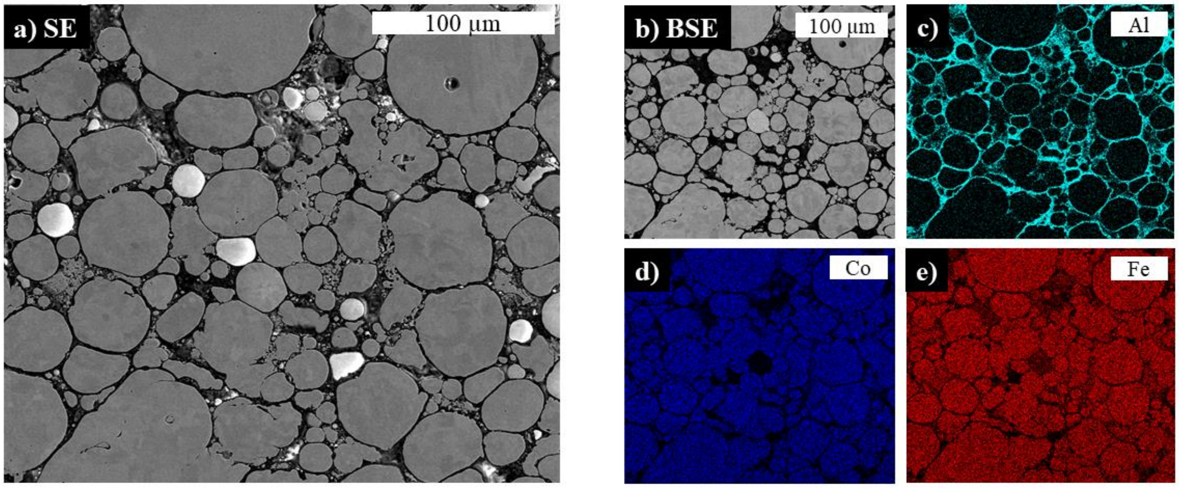

Figure 18. (a) Secondary electron micrograph and (b) corresponding backscatter electron micrograph and energy dispersive X-ray spectroscopy elemental maps of the 700°C consolidated CoFe – Al_2O_3 composite, showing the distinct, continuous Al_2O_3 coating surrounding CoFe powder particles.

The relative density of the 700°C consolidated composite was only approximately 82 %, relatively less dense than the 1000°C consolidated composite and appears more porous in the corresponding micrographs as well. From the SE micrograph in Figure 18 (a), porosity is observable within powder particle interiors, and between particles, in the Al_2O_3 coating. Compared to the 1000°C consolidated composite, the powders are more loosely packed in the 700°C consolidated composite. In the corresponding BSE micrograph, in Figure 18 (b), the Al_2O_3 phase, coating powder particles, appears nearly black and the CoFe particles appear light to medium gray with some contrast within powder particles due to grain orientation. The continuous Al_2O_3 coating of non-uniform thickness is observed between CoFe powder particles. Between particles, and at triple junctions especially, voids and gaps in the Al_2O_3 coating are observed. In the EDS element maps in Figure 18 (c), (d), and (e), no CoFe is detected in the Al_2O_3 coating regions between powder particles. A higher magnification SE micrograph and corresponding BSE micrograph is shown in Figure 19 (a) and (b), respectively.

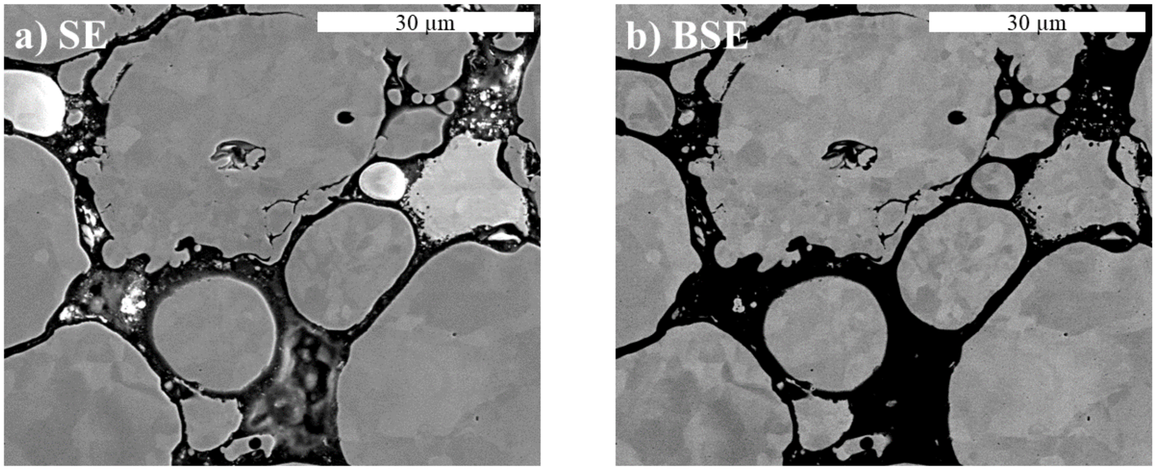

Figure 19. Higher magnification (a) secondary electron micrograph and (b) corresponding backscatter electron micrograph of the 700°C consolidated composite, showing non-uniformity in the Al_2O_3 coating surrounding CoFe powder particles.

In the SE micrographs in both Figures 18 (a) and 19 (a), powder particles bounded by Al_2O_3 coatings are observed to have an average particle size on the order of 10 µm. Within the powder particles, grain features are observed to be ~ 5 µm, as in the as-coated powders. Lastly, in the SE micrographs, some powder particles appear bright, but show no compositional difference in the corresponding BSE micrographs or EDS elemental maps in Figures 18 (b) – (e) and 19 (b).

4.3.3. Magnetic and electronic properties

The measured magnetic and electronic properties and relative densities of the consolidated CoFe – Al_2O_3 composites are reported in Table 5.

Table 5. Measured properties and relative densities of the consolidated CoFe – Al_2O_3 composites from this study, compared to previously reported properties of the CoFe alloy and other previously reported soft magnetic composites.

Sample	Saturation polarization (J_s) [T]	Coercivity (H_c) [A/m]	Through resistivity (ρ) [μΩ·m]	Relative density (% of theoretical)
1000°C SPS CoFe – Al_2O_3	1.90 ± 0.01	382 ± 6.1	0.20 ± 7.19	94.69 ± 0.24
700°C SPS CoFe – Al_2O_3	1.88 ± 0.01	98.9 ± 6.1	135.49 ± 7.19	82.54 ± 0.24
CoFe previous literature [8], [15], [21], [25], [26], [43]	2.3 – 2.4	10 - 1500	0.01 – 0.1	n.a.
SMC previous literature [8], [15], [29], [30], [80]–[83], [86]–[88]	0.3 – 1.5	150 – 400	100 – 30000	n.a.

Properties of the CoFe alloy and SMCs from previous literature are also shown in Table 5 for reference. While the 1000°C consolidated composite reached a measured J_s of 1.90 T, slightly higher than the J_s reported for the 700°C consolidated composite, both had noticeably greater J_s than previous SMCs, but not compared to the CoFe alloy. The 700°C sample achieved an electrical resistivity several orders of magnitude higher than the CoFe alloy and the 1000°C consolidated CoFe – Al_2O_3 composite from this work. The coercivity of the 700°C CoFe – Al_2O_3 composite was approximately an order of magnitude less than the composite consolidated at 1000°C. In previous literature of SMCs, far greater resistivities were achieved, at the cost of lowered J_s. Ultimately, in this study, the J_s of the composites was slightly lowered compared to the equiatomic CoFe alloy, but remained higher than that of SMCs produced in previous studies [30], [80]. In this study, compared to the 1:1 ratio by weight compared to the 1:1 ratio by weight CoFe alloy, a dramatically increased resistivity was achieved by consolidating Al_2O_3 coated CoFe powders. However, the electrical resistivity achieved in this SMC is within typical limits of previous SMC studies.

4.4. Discussion

4.4.1. 1000°C consolidation behavior and microstructural evolution

The 1000°C consolidated composite achieved high relative density, nearly 95 %, and is attributed to the high temperature SPS consolidation of the powders. There may be some discrepancy in the calculated relative density and the observed porosity in the SE micrographs because the phase fraction of Al_2O_3 was taken to be 2 vol. % Al_2O_3 but was not quantitively confirmed in this study. In the SE micrographs in Figures 16 (a) and 17 (a), the porosity observed within powder particles is on the nanometer scale and is common in gas atomized powders not fully densified [25], [39]. At 1000°C, ½ T_{melt} of Al_2O_3 and 2/3 T_{melt} of CoFe was reached. Also, any thermal expansion of the graphite SPS dies during SPS consolidation was not accounted for and caused increased uniaxial pressure, up to approximately 210 MPa. This high temperature and pressure are attributed to the elongation and tight packing of powder particles as well as diffusion of CoFe into the Al_2O_3 coating. At a temperature above ½ T_{melt} in metals, grain growth is expected and was observed in the 1000°C consolidated composite [89]. The consolidation of the CoFe – Al_2O_3 composite at 1000°C, relatively high temperature, is attributed to grain growth within the CoFe powder. Furthermore, at temperatures above 900°C, the α-BCC CoFe phase transforms to a γ-FCC CoFe phase, as shown in the phase diagram in Figure 3. During this phase transformation to FCC and back to BCC, further grain growth is likely to occur [89]. While CoFe and Al_2O_3 do not appear to have formed any new phase, as shown by the XRD pattern of the consolidated composite in Figure 15, at this temperature, it is likely that CoFe has started diffusing into and through regions of the Al_2O_3 coating. In the BSE micrographs in Figure 17 (b), CoFe is observed in some of the regions between CoFe particles, replacing some of the Al_2O_3 coating, suggesting the diffusion of CoFe into the particle boundary region. While the Al_2O_3 coating mostly prevented coalescence of and grain growth across powder particles, some CoFe may have diffused into the Al_2O_3 coating. It is possible the features seen in SE micrographs of the 1000°C composite, and described above, are artifacts of the mechanical polishing process, causing the Al_2O_3 coating to appear broken up and CoFe to appear within the coating between powder particles. However, the low resistivity measured in this sample would further suggest the diffusion of CoFe into the coating between powder particles. Further analysis with HRTEM EDS, electron diffraction, or electron probe microanalysis may be conducted to study the diffusion of CoFe in Al_2O_3.

In the XRD pattern of the 1000°C consolidated composite, an additional peak was expected, indicating the presence of Al_2O_3, but was not observed. The peaks which were observed are relatively narrow due to the coarse grain sizes and minimal strain in the consolidated and as-coated powders. The diffusion of CoFe into the coated particle boundary regions may account for the absence of an Al_2O_3 peak in the XRD pattern. Only 2 vol. % Al_2O_3 was coated on the CoFe particles which is near the limit of detection for XRD analysis and may also account for the absence of an Al_2O_3 peak in the XRD pattern. It is also possible the absence of an Al_2O_3 peak in the XRD pattern may suggest some Al is in solution with CoFe. Atomic diffusion of CoFe or Al may have occurred when the composite was consolidated at 1000°C, but XRD alone does not have the resolution to confirm which, if any, elements diffused at all.

In the SE and BSE micrographs of the 1000°C consolidated composites, morphological barriers ranging up to approximately 10 μm thick in Figures 16 (a) and (b) and 17 (a) and (b), were observed but no compositional difference in the barriers was observed in EDS elemental maps and as stated previously, no new phase was detected in XRD. Grain orientations in the CoFe powder cores seem to extend through these barrier regions, up to the particle boundary coating. Due to this and the fact the barrier seems to have a rough surface topology, observable in SE micrographs in Figures 16 (a) and 17 (a), the barriers are most likely artifacts from polishing. Ultimately, at 1000°C, the CoFe – Al_2O_3 composite was consolidated to near full density. Noticeable CoFe diffusion into the Al_2O_3 coating boundaries between particles most likely occurred at this temperature, but no formation of a new phase was observed. Further in-depth analysis of CoFe or Al diffusion requires HRTEM EDS, electron diffraction, or electron probe microanalysis.

4.4.2. 700°C consolidation behavior and microstructural evolution

In the XRD pattern of the 700°C consolidated composite in Figure 15, the major BCC CoFe peaks and an additional peak at a 2θ angle of 42.764° was observed. From previous literature, the additional peak most likely corresponds to the hexagonal α phase of Al_2O_3 [90]. However, a different set of additional peaks appear in the XRD pattern of the as-coated powders, at 2θ angles of 40.2859° and 44.097°. The extra peaks in the as-coated powder most likely correspond to the metastable cubic γ phase of Al_2O_3 [90]. The Al_2O_3 coating most likely undergoes a phase transformation from the metastable γ phase to the stable hexagonal α phase, which has been shown to occur at elevated temperatures and pressures in several previous works [90]–[92]. Additionally, the proprietary chemical vapor deposition powder coating process is a non-equilibrium process which potentially resulted in the deposition of a metastable Al_2O_3 phase on the CoFe powder particles. From the XRD pattern in Figure 15, after consolidation at 700°C, no evidence of formation of a new CoFe – Al_2O_3 phase was observed.

Compared to the composite consolidated at 1000°C, after consolidating the coated powders at 700°C, little to no grain growth was observed in the SE micrographs in Figures 18 (a) and 19 (a). At only 700°C, the Al_2O_3 coating only reached 0.35 its T_{melt} and most likely prevented full sintering and consolidation of the coated CoFe particles [25], [39]. The large gaps and voids observed between particles in the continuous Al_2O_3 coating are indicative of only partial densification. While some gaps and voids are from particles which have fallen out of the sample during polishing, the fact some particles are loosely bound at all further suggests the coated powder was not fully consolidated at 700°C. Furthermore, the loose packing of the CoFe powder particles and thicker, more substantial Al_2O_3 phase at triple junctions between particles, also suggests the powder particles were not fully densified. Additionally, the particles which appear brighter in SE micrographs in Figures 18 (a) and 19 (a) most likely emit high SE signal due to charging effects of trapped electrons in SEM [1]. These particles are most likely also loosely bound and potentially able to fall out, preventing the flow of electrons into the rest of the microscopy sample. It is also possible the powder particles are well electrically insulated and isolated from the rest of the sample, also preventing the flow of electrons from the SEM beam. In either case, the presence of the bright particles further suggests incomplete densification of the coated powder particles at only 700°C. Ultimately, at only 700°C, a continuous Al_2O_3 phase intersecting CoFe particles was achieved and no new phases in the CoFe – Al_2O_3 composite were detected. However, the composite was not fully densified. Despite the incomplete densification of the CoFe – Al_2O_3 composite at 700°C, exceptional magnetic and electronic properties were observed.

4.4.3. Magnetic behavior of the CoFe – Al_2O_3 soft magnetic composites

In Table 5, the magnetic properties of the 1000°C and 700°C consolidated composite showed only minor changes compared to the CoFe alloy and are attributed to microstructural features of the material. First of all, the exceptionally high J_s achieved in the CoFe alloy is attributed to the B2 ordered BCC CoFe structure [6], [21]. The ordering of the CoFe alloy occurs below 700°C and after cooling, therefore both consolidated composites would contain B2 ordered CoFe powder particles. However, the loose packing of powder particles can cause detrimental decreases to the J_s. The empty space and gaps between magnetic particles can prevent full magnetic alignment of domain walls in separated magnetic particles [7]–[9]. By physically separating CoFe particles, the Al_2O_3 phase reduces the bulk J_s of the composite. This effect is more noticeable in the 700°C consolidated composite as it is not fully densified, unlike the 1000°C consolidated composite which reached a higher density. However, both consolidated composites in this study achieved higher J_s than in previous SMCs and is attributed to the CoFe powder particles and relatively high densification achieved using SPS. Because full densification was achieved in the 1000°C composite, 1.90 T may be the maximum threshold J_s for this composite without reducing the volume fraction of Al_2O_3. From this J_s of 1.90 T, using a law of mixtures calculation, it is estimated there is approximately 20 % Al_2O_3 by volume in this SMC. The discrepancy from the targeted volume fraction of Al_2O_3 coated on CoFe powders is likely due to the broad particle size range consolidated in this study. Further improvement to the magnetic properties of the composite may be achieved by consolidating coated powders above a specific size range, effectively reducing the volume fraction of Al_2O_3 in the consolidated composite. In general, decreases to J_s in SMCs compared to the equiatomic CoFe alloy are expected and can be controlled with densification and Al_2O_3 volume fractions. The J_s reported of the SMCs in this study are exceptionally high compared to previous studies of SMCs and can be further improved upon in the future.

Similarly, the additional phase in a SMC can detrimentally cause increases in coercivity and therefore increased hysteresis losses. While the coercivity of the consolidated composites was not specifically targeted, the coercivity of the consolidated composites in this work was relatively low and in typical range of most SMCs. In general, larger grain sizes in soft magnetic materials typically results in decreased coercivities [8], [30], [80]. Despite this, the 1000°C consolidated composite displayed a relatively higher coercivity than the composite consolidated at 700°C, which experienced less grain growth. It is possible small CoFe pathways which diffused into the Al_2O_3 coating cause disruptions to the magnetization reversal of the larger powder particles of the composite. It is also possible the coercivity reported for the 1000°C consolidated composite is not statistically significant. Nonetheless, the coercivity is typical of consolidated SMCs. Although not reported, the relative permeability, which was not directly targeted or studied was on the order of approximately 3 in both consolidated composites. Compared to CoFe, the relative permeability of the consolidated composites in this work is relatively low and less than ideal, although process and Al_2O_3 volume fraction adjustments could improve the relative permeability substantially. Ultimately, the coercivity and permeability of the composites produced in this study fall in the range of typical magnetic coercivities and permeabilities of previously studied SMCs.

4.4.4. Electronic behavior of the CoFe – Al_2O_3 soft magnetic composites

The increased electrical resistivity of the CoFe – Al_2O_3 can be attributed to the Al_2O_3 coating, similar to the observed changes in magnetic properties. In the 1000°C consolidated composite, compared to the CoFe alloy, only a minor increase, within statistical variance of CoFe alloys is observed. As depicted in Figures 16 (b) and 17 (b), and discussed previously, during SPS consolidation at 1000°C, Co and Fe atoms most likely diffuse into localized regions of the Al_2O_3 coating between powder particles. This diffusion of CoFe most likely introduced electrically conductive pathways between particles, allowing charge carrier conduction across the Al_2O_3 boundaries between powder particles. Additionally, the larger grain sizes observed in the 1000°C sample further decrease scattering events of charge carriers, decreasing electrical resistivity, although this would not account for a several order of magnitude difference [34]. Compared to previously reported SMCs, the electrical resistivity of the CoFe – Al_2O_3 composite consolidated at 1000°C is relatively low. Ultimately, large increases in electrical resistivity were not observed in the 1000°C consolidated composite likely because CoFe diffused into Al_2O_3 boundaries between particles. To further increase the resistivity, the diffusion of CoFe into the insulating phase must be prevented.

By contrast, in the 700°C consolidated composite, the resistivity increased by nearly 4 orders of magnitude compared to the CoFe alloy. The dramatic increase to electrical resistivity is attributed to the retention of a continuous Al_2O_3 coating during SPS consolidation with no diffusion of constituent elements, and the relatively low density of the composite. Compared to previously reported SMCs, the electrical resistivity reported in the composite consolidated at 700°C is relatively low, but still within the typical range of properties. As discussed previously and shown in Figures 18 (a) and (b) and 19 (a) and (b), at 700°C, the composite was only partially densified. During SPS consolidation at 700°C, the CoFe particles remained fully bounded by the Al_2O_3 coating, effectively creating a continuous, porous phase of Al_2O_3 through the CoFe particles. The irregularities in the morphology of the Al_2O_3 phase at triple junctions and between particles prevents charge carrier conduction, increasing the bulk electrical resistivity measured through the composite. This increased resistivity can result in the reduction of eddy current losses of transformer cores by minimizing eddy currents in the bulk composite. Additionally, eddy current losses are further reduced by limiting the electrical domain size d to the size of coated powder particles as discussed with Equation 1 previously. If eddy currents are produced in the bulk composite, the eddy current sizes will be confined to individual CoFe powder particles and significant eddy current losses can be prevented. Ultimately, dramatic increases to resistivity in the 700°C consolidated composite, compared to the composite consolidated at 1000°C and CoFe alloy are attributed to the SMC having a relatively low density and a fully continuous Al_2O_3 phase separating CoFe powder particles with no CoFe diffusion into that phase.

4.5. Summary

A CoFe – Al_2O_3 composite was produced by consolidating Al_2O_3 coated CoFe powder particles via SPS, targeting a SMC with high J_s and high electrical resistivity. The powder particles were coated with a large-scale, proprietary coating deposition process. After consolidating the coated powders at 1000°C, only minor changes to the magnetic and electronic properties were observed, compared to the CoFe alloy, and were attributed to CoFe diffusion into the Al_2O_3 coatings between powder particles. The composite consolidated at 700°C displayed an exceptional combination of high J_s, 1.88 T, and high electrical resistivity, 135 μΩ·m, and the properties were attributed to the SMC having relatively low density and a continuous Al_2O_3 coating surrounding CoFe powder particles. Further densification of the CoFe – Al_2O_3 composite after consolidation at 700°C, without uncontrolled CoFe diffusion, may further improve magnetic and electronic properties of the composite. In the future, the consolidation of larger powder particle size ranges can reduce the volume fraction of Al_2O_3 and further target improved soft magnetic properties. However, larger powder particle sizes and therefore lowered Al_2O_3 volume fractions may result in reduced electrical resistivity. In this study, the focus was magnetic and electronic properties of these consolidated composites; future studies exploring mechanical behavior of the composite is recommended to further develop the CoFe – Al_2O_3 composite and others like it for widespread transformer core applications. The efficiency of soft magnetic materials may be increased by controlling secondary phase fractions and morphologies and constituent element diffusion in SMCs.

Chapter 5: Concluding Comments

A systematic approach to the microstructural design and development of CoFe – based soft magnetic materials for more resilient, power dense, and efficient transformer cores was undertaken. A critical understanding of the microstructural features in CoFe systems and their impact on the system's magnetic and electronic properties is identified as a critical aspect for developing improved soft magnetic transformer cores. To this end, several studies of targeted microstructures in CoFe – based alloys were conducted to investigate the relationship between microstructural features and measured magnetic and electronic properties.

The first study was the development of a nanocrystalline, solid solution CoFe – P alloy to target a soft magnetic transformer core material with more efficient magnetic and electronic properties. Through the detailed study of the CoFe system and unstable microstructural features in CoFe – P films, a systematic approach to the synthesis of a bulk CoFe – P alloy with similar microstructures using established non-equilibrium powder metallurgical techniques was utilized. Mechanical alloying, followed by 700°C SPS consolidation of a low P concentration CoFe alloy successfully resulted in an alloy with a nanocrystalline, solid solution microstructure, but revealed little to no changes in magnetic and electronic properties compared to a similarly processed CoFe alloy with no P. Using the same processes, a high P concentration CoFe alloy was produced, but a stable, intermetallic $(Co_{1-x}Fe_x)_2P$ phase precipitated during SPS consolidation and was unavoidable even at lower temperatures, likely due to extremely low solubility of P in the alloy and thermodynamic stability of the intermetallic. The precipitated intermetallic phase was found to be detrimental to the final magnetic properties of the alloy and was attributed to the hard or permanent magnetic properties of the intermetallic phase. Ultimately, compared to the non-equilibrium film deposition techniques utilized by Taslimi and Kalu, the high temperatures experienced during SPS consolidation bring the alloy closer to equilibrium and prevented the retention of a supersaturated solid solution formed in the powders during mechanical alloying [32], [33]. The use of far from equilibrium processing techniques are necessary to develop a CoFe – based alloy for more efficient soft magnetic transformer core materials.

The second investigation focused on the impact of typical LENS® additive manufactured columnar grain microstructures on the magnetocrystalline anisotropic behavior of the equiatomic CoFe alloy. The CoFe alloy was deposited with the repeated LENS® process parameter but varied laser power settings. At all laser power settings, the CoFe alloy was deposited with typical columnar grain microstructures of LENS® additive manufacturing and reached nearly full densification. However, practically no effect of the magnetocrystalline behavior of the CoFe alloy was observed. The relatively isotropic behavior of the LENS® deposited CoFe alloy was attributed to the high symmetry of the B2 ordered BCC structure of the CoFe alloy and the lack of crystallographic texturing from the LENS® process. By using a 90° hatch rotation LENS® parameter, the columnar grains were randomly oriented in the CoFe alloys. To achieve a crystallographically textured deposited alloy, 0° hatch rotation LENS® parameters can be used to grow columnar grains epitaxially, ultimately maintaining a crystallographic orientation through the deposited alloys. By controlling LENS® parameters and therefore the solidification front of the metal additive manufacturing process, the microstructure, and specifically texture, of CoFe – based alloys can be controlled to unlock more efficient magnetic behavior of the alloy.

In the final study, a CoFe – based SMC with a continuous non-magnetic phase, fully intersecting CoFe particles was targeted to produce a more efficient soft magnetic transformer core. The morphology and distribution of the non-magnetic phase was aimed at producing a material with high electrical resistivity, without sacrificing high J_s. Using a proprietary film deposition technique, equiatomic CoFe powder particles were coated with Al_2O_3 and the coated powders were subsequently SPS consolidated at various temperatures. In the consolidated CoFe – Al_2O_3 SMCs, no new phases were formed and the CoFe powder core and Al_2O_3 powder particle coating, bounding particles were retained through SPS consolidation. In the consolidated SMC, a CoFe phase, fully intersected by a continuous, non-magnetic Al_2O_3 phase was achieved. At high temperature, CoFe was revealed to diffuse into the Al_2O_3 coating on particle boundaries and was found to be detrimental to the measured electronic properties of the SMC, resulting in a relatively low electrical resistivity. After consolidating the CoFe – Al_2O_3 SMC at relatively lower temperatures, the diffusion of CoFe was avoided and the electrical resistivity of the SMC was increased four orders of magnitude compared to the CoFe alloy and achieved exceptionally high J_s compared to previously reported SMCs. A CoFe – based SMC with a continuous non-magnetic phase fully intersecting CoFe phase particles was successfully consolidated using SPS and achieved exceptional soft magnetic and electronic properties for use as a more efficient transformer core material.

Chapter 6: Recommendations for future work

This work makes significant headway in the field of soft magnetic materials for improved transformer cores and better develops an understanding of microstructural features of CoFe – based alloys and their relationships with the magnetic and electronic properties of the alloy. Critical findings from this work can lead key directions essential for the growth of CoFe – based soft magnetic transformer core materials. These include the application of complex concentrated alloy design and the application of interfacial engineering to develop CoFe – based alloys with the microstructures necessary for improved soft magnetic properties.

The design concepts for complex concentrated alloys can enable the production of CoFe – based alloys which can more easily achieve the microstructural features necessary for improved soft magnetic properties. The microstructural features for improved soft magnetic materials, such as the B2 ordered BCC CoFe structure, are well documented, but real materials with those microstructures can often be difficult to produce. Using complex concentrated alloy design approaches, CoFe – based alloys with stabilized B2 ordered or solid solution BCC phases can be developed and more easily targeted using non-equilibrium processing techniques. Predictive complex concentrated alloy design tools, such as CALPHAD can be used to determine the processing conditions necessary to achieve the non-equilibrium microstructures beneficial to soft magnetic properties. However, the CALPHAD databases must be further developed to include non-metallic elements useful in magnetically ordered alloys. Complex concentrated alloy design concepts can be used to drive the processing conditions for efficient soft magnetic materials.

In addition to complex concentrated alloy design, the application of interfacial engineering can further lead development of materials with microstructures necessary for more efficient soft magnetic transformer cores. While the B2 ordered BCC CoFe phase yields exceptional magnetic properties, an intersecting non-magnetic phase was found to yield beneficial electronic properties in SMCs. By applying interfacial science to complex CoFe – based alloys, an intersecting phase along interfaces such as grain boundaries can be designed to provide similar beneficial electronic properties as the non-magnetic particle boundary phase in SMCs. A smaller phase at grain boundaries can potentially have less detrimental effect on the measured magnetic properties of the bulk alloy, but further research surrounding the effects of a grain boundary phase on magnetic properties are necessary. Through the application of interfacial engineering, a new design approach to SMCs and soft magnetic materials can be realized, producing more efficient transformer core materials.

REFERENCES

[1] W. Callister and D. Rethwisch, *Materials Science & Engineering An Introduction*, 8th Ed. Hoboken: Wiley, 2010.

[2] *National Fire Protection Association 70 National Electrical Code*. USA, 2014, pp. 1–15. Accessed: Nov. 19, 2020. [Online]. Available: http://www.madcad.com/library/182159/557177/

[3] “U.S. energy facts explained - consumption and production - U.S. Energy Information Administration (EIA).” https://www.eia.gov/energyexplained/us-energy-facts/ (accessed Nov. 19, 2020).

[4] “Monthly Energy Review – October 2020,” Washington, DC, 2020. Accessed: Nov. 19, 2020. [Online]. Available: www.eia.gov/mer

[5] J. S. Foster, E. Gjelde, and W. Graham, “Report of the Commission to Assess the Threat to the US from EMP Attack,” 2008.

[6] A. M. Leary, P. R. Ohodnicki, and M. E. Mchenry, “Soft magnetic materials in high-frequency, high-power conversion applications,” *Jom*, Vol. 64, No. 7, pp. 772–781, 2012, doi: 10.1007/s11837-012-0350-0.

[7] J. G. Webster, *Wiley Encyclopedia of Electrical and Electronics Engineering*. Wiley, 2016. doi: 10.1002/047134608x.

[8] J. M. Silveyra, E. Ferrara, D. L. Huber, and T. C. Monson, “Soft magnetic materials for a sustainable and electrified world.,” *Science (New York, N.Y.)*, Vol. 362, No. 6413, Oct. 2018, doi: 10.1126/science.aao0195.

[9] K. M. Krishnan, *Fundamentals and Applications of Magnetic Materials*, 1st Ed. Oxford: Oxford University Press, 2016.

[10] B. D. Cullity and C. D. Graham, *Introduction to Magnetic Materials*, Second. Piscataway, NJ: Wiley, 2009.

[11] G. Herzer, “Soft Magnetic Materials—Nanocrystalline Alloys,” in *Handbook of Magnetism and Advanced Magnetic Materials*, Chichester, UK: John Wiley & Sons, Ltd, 2007. doi: 10.1002/9780470022184.hmm402.

[12] S. Jeszenszky, “History of Transformers,” *IEEE Power Engineering Review*, Vol. 16, No. 12, p. 9, 1996, doi: 10.1109/MPER.1996.546444.

[13] M. Guarnieri, “Who Invented the Transformer?,” *IEEE Industrial Electronics Magazine*, pp. 56–59, 2013.

[14] A. Campbell, “On the Magnetic Properties of Silicon Iron (Stalloy) in Alternating Magnetic Fields of Low Value,” *Proceedings of the Physical Society of London*, Vol. 32, pp. 232–243, 1919.

[15] G. Ouyang, X. Chen, Y. Liang, C. Macziewski, and J. Cui, “Review of Fe-6.5 wt%Si high silicon steel—A promising soft magnetic material for sub-kHz application,” *Journal of Magnetism and Magnetic Materials*, Vol. 481. Elsevier B.V., pp. 234–250, Jul. 01, 2019. doi: 10.1016/j.jmmm.2019.02.089.

[16] V. R. V. Ramanan, “Metallic glasses in distribution transformer applications: An update,” *Journal of Materials Engineering*, Vol. 13, No. 2, pp. 119–127, 1991, doi: 10.1007/BF02995816.

[17] H. X. Li, Z. C. Lu, S. L. Wang, Y. Wu, and Z. P. Lu, “Fe-based bulk metallic glasses: Glass formation, fabrication, properties and applications,” *Progress in Materials Science*, Vol. 103, No. December 2018, pp. 235–318, 2019, doi: 10.1016/j.pmatsci.2019.01.003.

[18] C. Suryanarayana and A. Inoue, “Iron-based bulk metallic glasses,” *International Materials Reviews*, Vol. 58, No. 3, pp. 131–166, Apr. 2013, doi: 10.1179/1743280412Y.0000000007.

[19] P. Weiss, “The magnetic properties of the alloys of the ferromagnetic metals: iron-nickel, nickel-cobalt, cobalt-iron,” *Transactions of the Faraday Society*, Vol. 8, pp. 149–156, 1912.

[20] I. Ohnuma, H. Enoki, O. Ikeda, R. Kainuma, H. Ohtani, B. Sundman, and K. Ishida, “Phase equilibria in the Fe-Co binary system,” *Acta Materialia*, Vol. 50, No. 2, pp. 379–393, 2002, doi: 10.1016/S1359-6454(01)00337-8.

[21] T. Sourmail, “Near equiatomic FeCo alloys: Constitution, mechanical and magnetic properties,” *Progress in Materials Science*, Vol. 50, No. 7. pp. 816–880, Sep. 2005. doi: 10.1016/j.pmatsci.2005.04.001.

[22] J. K. Stanley and T. D. Yensen, “Hiperco - A Magnetic Alloy,” *AIEE Transactions*, Vol. 66, pp. 714–7187, 1947, doi: 10.1017/CBO9781107415324.004.

[23] K. B. Shedd and A. Hwang, “Mineral Industry Surveys,” Reston, VA, 2020.

[24] J. F. Slack, B. E. Kimball, and K. B. Shedd, “Cobalt,” Washington, DC, 2017. [Online]. Available: https://doi.org/10.3133/pp1802F

[25] A. Dupuy, B. Zheng, Y. Zhou, J. Delplanque, T. Monson, E. J. Lavernia, and J. M. Schoenung, “Consolidation and Behavior of FeCoV Soft Magnetic Materials via Spark Plasma Sintering,” in *Spark Plasma Sintering of Materials*, P. Cavaliere, Ed. Lecce: Springer, 2019, pp. 473–491. doi: 10.1007/978-3-030-05327-7.

[26] H. Moumeni, S. Alleg, and J. M. Greneche, “Structural properties of Fe50Co50 nanostructured powder prepared by mechanical alloying,” *Journal of Alloys and Compounds*, Vol. 386, No. 1–2, pp. 12–19, Jan. 2005, doi: 10.1016/j.jallcom.2004.05.017.

[27] H. Moumeni, S. Alleg, C. Djebbari, F. Z. Bentayeb, J. M. Gren`eche, and G. Gren`eche, “Synthesis and characterisation of nanostructured FeCo alloys,” *Journal of Materials Science*, Vol. 39, pp. 5441–5443, 2004, Accessed: Jul. 23, 2019. [Online]. Available: https://link.springer.com/content/pdf/10.1023%2FB%3AJMSC.0000039262.37788.b7.pdf

[28] R. S. Sundar and S. C. Deevi, *Soft magnetic FeCo alloys: Alloy development, processing, and properties*, Vol. 50, No. 3. 2005. doi: 10.1179/174328005X14339.

[29] H. Shokrollahi and K. Janghorban, “Soft magnetic composite materials (SMCs),” *Journal of Materials Processing Technology*, Vol. 189, No. 1–3, pp. 1–12, 2007, doi: 10.1016/j.jmatprotec.2007.02.034.

[30] E. A. Périgo, B. Weidenfeller, P. Kollár, and J. Füzer, “Past, present, and future of soft magnetic composites,” *Applied Physics Reviews*, Vol. 5, No. 3, 2018, doi: 10.1063/1.5027045.

[31] D. Goll, D. Schuller, G. Martinek, T. Kunert, J. Schurr, C. Sinz, T. Schubert, T. Bernthaler, H. Riegel, and G. Schneider, “Additive manufacturing of soft magnetic materials and components,” *Additive Manufacturing*, Vol. 27, No. March, pp. 428–439, 2019, doi: 10.1016/j.addma.2019.02.021.

[32] E. E. Kalu, “Properties of nanocrystalline electrodeposited CoFeP alloy with low phosphorus content,” *Journal of Solid State Electrochemistry*, Vol. 11, No. 9, pp. 1145–1156, 2007, doi: 10.1007/s10008-006-0252-6.

[33] H. Taslimi, M. Heydarzadeh Sohi, S. Mehrizi, and M. Saremi, “Studies of the effects of addition of P and Cr on microstructure and electrical resistivity of nanocrystalline CoFe thin films,” *Journal of Materials Science: Materials in Electronics*, Vol. 26, No. 5, pp. 2962–2968, 2015, doi: 10.1007/s10854-015-2783-z.

[34] S. Kasap, C. Koughia, H. Ruda, C. Tannous, and J. Gieraltowski, *Electronic and Photonic Materials*, 2nd Ed. Cham: Springer International Publishing, 2017. doi: 10.1007/978-3-319-48933-9_4.

[35] H. Okamoto, “The Fe-P (iron-phosphorus) system,” *Bulletin of Alloy Phase Diagrams*, Vol. 11, No. 4, pp. 404–412, 1990, doi: 10.1007/BF02843320.

[36] M. H. Enayati and F. A. Mohamed, “Application of mechanical alloying/milling for synthesis of nanocrystalline and amorphous materials,” *International Materials Reviews*, Vol. 59, No. 7, pp. 394–416, 2014, doi: 10.1179/1743280414Y.0000000036.

[37] C. Suryanarayana, “Mechanical alloying and milling,” *Progress in Materials Science*, Vol. 46, No. 1–2. pp. 1–184, 2001. doi: 10.1016/S0079-6425(99)00010-9.

[38] R. H. R. Castro and K. Van Benthem, *Sintering*, Vol. 35, No. 3. London: Springer, 2013. doi: 10.1080/08940886.2017.1316123.

[39] J. E. Garay, “Current-Activated, Pressure-Assisted Densification of Materials,” *Annual Review of Materials Research*, Vol. 40, pp. 445–468, 2010, doi: 10.1146/annurev-matsci-070909-104433.

[40] Y. Do Kim, J. Y. Chung, J. Kim, and H. Jeon, “Formation of nanocrystalline Fe-Co powders produced by mechanical alloying,” *Materials Science and Engineering A*, Vol. 291, No. 1, pp. 17–21, 2000, doi: 10.1016/S0921-5093(00)00982-5.

[41] Q. Zeng, I. Baker, V. McCreary, and Z. Yan, “Soft ferromagnetism in nanostructured mechanical alloying FeCo-based powders,” *Journal of Magnetism and Magnetic Materials*, Vol. 318, No. 1–2, pp. 28–38, Nov. 2007, doi: 10.1016/j.jmmm.2007.04.037.

[42] R. Elkalkouli, M. Grosbras, and J. F. Dinhut, “Mechanical and magnetic properties of nanocrystalline FeCo alloys produced by mechanical alloying,” *Nanostructured Materials*, Vol. 5, No. 6, pp. 733–743, 1995, doi: 10.1016/0965-9773(95)00283-K.

[43] A. Zeleňáková, D. Olekšáková, J. Degmová, J. Kováč, P. Kollár, M. Kusý, and P. Sovák, “Structural and magnetic properties of mechanically alloyed FeCo powders,” *Journal of Magnetism and Magnetic Materials*, Vol. 316, No. 2, 2007, doi: 10.1016/j.jmmm.2007.03.005.

[44] J. B. Nelson and D. P. Riley, “An experimental investigation of extrapolation methods in the derivation of accurate unit-cell dimensions of crystals,” *Proceedings of the Physical Society*, Vol. 57, No. 3, pp. 160–177, 1945, doi: 10.1088/0959-5309/57/3/302.

[45] M. De Graef and M. E. McHenry, *Structure of Materials an Introduction to Crystallography, Diffraction, and Symmetry*, 2nd Ed. Cambridge University Press, 2012.

[46] D. W. Clegg and R. A. Buckley, “The Disorder → Order Transformation in Iron-Cobalt-Based Alloys,” *Metal Science Journal*, Vol. 7, No. 1, pp. 48–54, 1973, doi: 10.1179/030634573790445541.

[47] A. S. Normanton, P. E. Bloomfield, F. R. Sale, and B. B. Argent, “A Calorimetric Study of Iron–Cobalt Alloys,” *Metal Science*, Vol. 9, No. 1, pp. 510–517, 1975, doi: 10.1179/030634575790444658.

[48] A. B. Kustas, D. F. Susan, K. L. Johnson, S. R. Whetten, M. A. Rodriguez, D. J. Dagel, J. R. Michael, D. M. Keicher, and N. Argibay, “Characterization of the Fe-Co-1.5V soft ferromagnetic alloy processed by Laser Engineered Net Shaping (LENS),” *Additive Manufacturing*, Vol. 21, pp. 41–52, May 2018, doi: 10.1016/J.ADDMA.2018.02.006.

[49] J. Fu, J. C. Brouwer, I. M. Richardson, and M. J. M. Hermans, “Effect of mechanical alloying and spark plasma sintering on the microstructure and mechanical properties of ODS Eurofer,” *Materials and Design*, Vol. 177, No. 107849, 2019, doi: 10.1016/j.matdes.2019.107849.

[50] M. S. Staltsov, I. I. Chernov, I. A. Bogachev, B. A. Kalin, E. A. Olevsky, L. J. Lebedeva, and A. A. Nikitina, “Optimization of mechanical alloying and spark-plasma sintering regimes to obtain ferrite–martensitic ODS steel,” *Nuclear Materials and Energy*, Vol. 9, pp. 360–366, 2016, doi: 10.1016/j.nme.2016.08.020.

[51] R. Fruchart, A. Roger, and J. P. Senateur, “Crystallographic and magnetic properties of solid solutions of the phosphides M2P, M = Cr, Mn, Fe, Co, and Ni,” *Journal of Applied Physics*, Vol. 40, No. 3, pp. 1250–1257, 1969, doi: 10.1063/1.1657617.

[52] S. Kumar, S. Chander, A. Krishnamurthy, and B. K. Srivastava, “Magnetic behaviour of alloys in the series (Fe1-xCox)2P,” *Journal of Magnetism and Magnetic Materials*, Vol.

237, No. 2, pp. 135–142, 2001, doi: 10.1016/S0304-8853(01)00489-9.

[53] S. K. Jain, S. Kumar, P. S. R. Krishna, A. B. Shinde, A. Krishnamurthy, and B. K. Srivastava, “Neutron diffraction study on the magnetic structure of (Fe0.70Co0.30)2P,” *Journal of Alloys and Compounds*, Vol. 439, No. 1–2, pp. 13–17, 2007, doi: 10.1016/j.jallcom.2006.08.258.

[54] K. J. De Vos, W. A. J. J. Velge, M. G. Van Der Steeg, and H. Zijlstra, “Permanent magnetic properties of iron-cobalt-phosphides,” *Journal of Applied Physics*, Vol. 33, No. 3, pp. 1320–1322, 1962, doi: 10.1063/1.1728712.

[55] K. Oikawa, G. W. Qin, T. Ikeshoji, R. Kainuma, and K. Ishida, “Co (Cobalt) Binary Alloy Phase Diagrams,” *Alloy Phase Diagrams*, Vol. 50, pp. 263–281, 2018, doi: 10.31399/asm.hb.v03.a0006156.

[56] G. E. Lloyd, “Atomic number and crystallographic contrast images with the SEM: a review of backscattered electron techniques,” *Mineralogical Magazine*, Vol. 51, No. 359, pp. 3–19, 1987, doi: 10.1180/minmag.1987.051.359.02.

[57] G. Herzer, “Modern soft magnets: Amorphous and nanocrystalline materials,” *Acta Materialia*, Vol. 61, No. 3, pp. 718–734, Feb. 2013, doi: 10.1016/j.actamat.2012.10.040.

[58] J. A. Bas, J. A. Calero, and M. J. Dougan, “Sintered soft magnetic materials. Properties and applications,” *Journal of Magnetism and Magnetic Materials*, Vol. 254, No. 255, pp. 391–398, 2003, doi: 10.1016/S0304-8853(02)00934-4.

[59] J. Iñiguez, C. Pereira, and J. Rivas, “Effect of porosity on the magnetic behaviour of nickel ferrites,” *Applied Physics A Solids and Surfaces*, Vol. 36, No. 3, pp. 159–161, 1985, doi: 10.1007/BF00624937.

[60] K. J. Sixtus, “Magnetic anisotropy in silicon steel,” *Journal of Applied Physics*, Vol. 6, No. 3, pp. 105–111, 1935, doi: 10.1063/1.1745294.

[61] R. H. Fowler and F. C. Powell, “A note on Ferromagnetism,” *Mathematical Proceedings of the Cambridge Philosophical Society*, Vol. 27, No. 2, pp. 280–289, 1931, doi: 10.1017/S0305004100010409.

[62] F. C. Powell, “The direction of magnetisation of single ferromagnetic crystals,” Vol. 228, No. 19, pp. 167–181, 1930.

[63] W. J. Sames, F. A. List, S. Pannala, R. R. Dehoff, and S. S. Babu, “The metallurgy and processing science of metal additive manufacturing,” *International Materials Reviews*, Vol. 61, No. 5, pp. 315–360, Jul. 2016, doi: 10.1080/09506608.2015.1116649.

[64] D. M. Keicher, J. E. Smugeresky, J. A. Romero, M. L. Griffith, and L. D. Harwell, “Using the laser engineered net shaping (LENS) process to produce complex components from a CAD solid model,” *SPIE*, Vol. 2993, No. March 1997, pp. 91–97, 1997, doi: 10.1117/12.270018.

[65] W. J. Sames, F. A. List, S. Pannala, R. R. Dehoff, and S. S. Babu, “The metallurgy and

processing science of metal additive manufacturing," *International Materials Reviews*, Vol. 61, No. 5, pp. 315–360, 2016, doi: 10.1080/09506608.2015.1116649.

[66] K. L. Terrassa, "An Investigation of the Reuse of Powder Feedstock, Process Parameters, and General Operational Procedures for Laser Engineered Net Shaping Additive Manufacturing," University of California, Irvine, 2017. [Online]. Available: https://escholarship.org/uc/item/1tr0c2p0

[67] T. F. Babuska, M. A. Wilson, K. L. Johnson, S. R. Whetten, J. F. Curry, J. M. Rodelas, C. Atkinson, P. Lu, M. Chandross, B. A. Krick, J. R. Michael, N. Argibay, D. F. Susan, and A. B. Kustas, "Achieving high strength and ductility in traditionally brittle soft magnetic intermetallics via additive manufacturing," *Acta Materialia*, Vol. 180, pp. 149–157, 2019, doi: 10.1016/j.actamat.2019.08.044.

[68] A. B. Kustas, C. M. Fancher, S. R. Whetten, D. J. Dagel, J. R. Michael, and D. F. Susan, "Controlling the extent of atomic ordering in intermetallic alloys through additive manufacturing," *Additive Manufacturing*, Vol. 28, No. February, pp. 772–780, 2019, doi: 10.1016/j.addma.2019.06.020.

[69] C. V. Mikler, V. Chaudhary, T. Borkar, V. Soni, D. Jaeger, X. Chen, R. Contieri, R. V. Ramanujan, and R. Banerjee, "Laser Additive Manufacturing of Magnetic Materials," *JOM*, Vol. 69, No. 3, pp. 532–543, Mar. 2017, doi: 10.1007/s11837-017-2257-2.

[70] V. Chaudhary, N. M. Sai Kiran Kumar Yadav, S. A. Mantri, S. Dasari, A. Jagetia, R. V. Ramanujan, and R. Banerjee, "Additive manufacturing of functionally graded Co–Fe and Ni–Fe magnetic materials," *Journal of Alloys and Compounds*, Vol. 823, p. 153817, 2020, doi: 10.1016/j.jallcom.2020.153817.

[71] W. Everhart and J. Newkirk, "Grain size effects in selective laser melted Fe-Co-2V," *Applied Sciences*, Vol. 9, 2019.

[72] K. L. Terrassa, J. C. Haley, B. E. MacDonald, and J. M. Schoenung, "Reuse of powder feedstock for directed energy deposition," *Powder Technology*, Vol. 338, pp. 819–829, 2018, doi: 10.1016/j.powtec.2018.07.065.

[73] K. L. Terrassa, T. R. Smith, S. Jiang, J. D. Sugar, and J. M. Schoenung, "Improving build quality in Directed Energy Deposition by cross-hatching," *Materials Science and Engineering A*, Vol. 765, No. August, p. 138269, 2019, doi: 10.1016/j.msea.2019.138269.

[74] W. Kurz, C. Bezençon, and M. Gäumann, "Columnar to equiaxed transition in solidification processing," *Science and Technology of Advanced Materials*, Vol. 2, No. 1, pp. 185–191, 2001, doi: 10.1016/S1468-6996(01)00047-X.

[75] J. D. Hunt, "Steady state columnar and equiaxed growth of dendrites and eutectic," *Materials Science and Engineering*, Vol. 65, No. 1, pp. 75–83, 1984, doi: 10.1016/0025-5416(84)90201-5.

[76] U. Scipioni Bertoli, A. J. Wolfer, M. J. Matthews, J. P. R. Delplanque, and J. M. Schoenung, "On the limitations of Volumetric Energy Density as a design parameter for

Selective Laser Melting," *Materials and Design*, Vol. 113, pp. 331–340, 2017, doi: 10.1016/j.matdes.2016.10.037.

[77] P. Kiani, A. D. Dupuy, K. Ma, and J. M. Schoenung, "Directed energy deposition of AlSi10Mg: Single track nonscalability and bulk properties," *Materials and Design*, Vol. 194, p. 108847, 2020, doi: 10.1016/j.matdes.2020.108847.

[78] A. Sola and A. Nouri, "Microstructural porosity in additive manufacturing: The formation and detection of pores in metal parts fabricated by powder bed fusion," *Journal of Advanced Manufacturing and Processing*, Vol. 1, No. 3, pp. 1–21, 2019, doi: 10.1002/amp2.10021.

[79] J. W. Shih, "Magnetic Properties of Iron-Cobalt Single Crystals," Yale University, 1934.

[80] K. J. Sunday and M. L. Taheri, "Soft magnetic composites: recent advancements in the technology," *Metal Powder Report*, Vol. 72, No. 6, pp. 425–429, 2017, doi: 10.1016/j.mprp.2016.08.003.

[81] R. H. Yu, S. Basu, L. Ren, Y. Zhang, A. Parvizi-Majidi, K. M. Unruh, and J. Q. Xiao, "High temperature soft magnetic materials: FeCO alloys and composites," *IEEE Transactions on Magnetics*, Vol. 36, No. 5 I, pp. 3388–3393, 2000, doi: 10.1109/20.908809.

[82] L. Svensson, K. Frogner, P. Jeppsson, T. Cedell, and M. Andersson, "Soft magnetic moldable composites: Properties and applications," *Journal of Magnetism and Magnetic Materials*, Vol. 324, No. 18, pp. 2717–2722, 2012, doi: 10.1016/j.jmmm.2012.03.049.

[83] M. M. Dias, H. J. Mozetic, J. S. Barboza, R. M. Martins, L. Pelegrini, and L. Schaeffer, "Influence of resin type and content on electrical and magnetic properties of soft magnetic composites (SMCs)," *Powder Technology*, Vol. 237, pp. 213–220, 2013, doi: 10.1016/j.powtec.2013.01.006.

[84] K. Sugimura, Y. Miyajima, M. Sonehara, T. Sato, F. Hayashi, N. Zettsu, K. Teshima, and H. Mizusaki, "Formation of high electrical-resistivity thin surface layer on carbonyl-iron powder (CIP) and thermal stability of nanocrystalline structure and vortex magnetic structure of CIP," *AIP Advances*, Vol. 6, No. 5, 2016, doi: 10.1063/1.4944705.

[85] T. Ishizaki, H. Nakano, S. Tajima, and N. Takahashi, "Improving powder magnetic core properties via application of thin, insulating silica-nanosheet layers on iron powder particles," *Nanomaterials*, Vol. 7, No. 1, pp. 1–13, 2017, doi: 10.3390/nano7010001.

[86] J. Zheng, H. Zheng, J. Lei, Y. Ying, L. Qiao, W. Cai, W. Li, J. Yu, Y. Tang, and S. Che, "Magnetic properties and microstructure of iron-based soft magnetic composites with Al2O3 insulating coating by one-pot synthesis method," *Journal of Magnetism and Magnetic Materials*, Vol. 499, p. 166255, 2020, doi: 10.1016/j.jmmm.2019.166255.

[87] K. J. Sunday, K. A. Darling, F. G. Hanejko, B. Anasori, Y. C. Liu, and M. L. Taheri, "Al2O3 'self-coated' iron powder composites via mechanical milling," *Journal of Alloys and Compounds*, Vol. 653, pp. 61–68, 2015, doi: 10.1016/j.jallcom.2015.08.260.

[88] Y. Peng, Y. Yi, L. Li, J. Yi, J. Nie, and C. Bao, “Iron-based soft magnetic composites with Al2O3 insulation coating produced using sol–gel method,” *Materials and Design*, Vol. 109, pp. 390–395, 2016, doi: 10.1016/j.matdes.2016.07.097.

[89] D. Porter, K. Easterling, and M. Sherif, *Phase Transformations in Metals and Alloys*, 3rd Ed. Boca Raton: CRC Press, 2009.

[90] F. R. Feret, D. Roy, and C. Boulanger, “Determination of alpha and beta alumina in ceramic alumina by X-ray diffraction,” *Spectrochimica acta, Part B: Atomic spectroscopy*, Vol. 55, No. 7, pp. 1051–1061, 2000, doi: 10.1016/S0584-8547(00)00225-1.

[91] C. Steiner, D. P. H. Hasselman, and R. M. Spriggs, “Kinetics of the Gamma-to-Alpha Alumina Phase Transformation,” *Journal of the American Ceramic Society,* Vol. 54, No. 8, pp. 412–413, 1971, doi: 10.1111/j.1151-2916.1971.tb12335.x.

[92] F. Balima and A. Largeteau, “Phase transformation of alumina induced by high pressure spark plasma sintering (HP-SPS),” *Scripta Materialia,* Vol. 158, pp. 20–23, 2019, doi: 10.1016/j.scriptamat.2018.08.016.